Published in final edited form as:
Nature. 2022 April 01; 604(7904): 190–194. doi:10.1038/s41586-022-04517-3.

Differential assembly diversifies $GABA_A$ receptor structures and signalling

Andrija Sente[1,*], **Rooma Desai**[2], **Katerina Naydenova**[1], **Tomas Malinauskas**[3], **Youssef Jounaidi**[2], **Jonas Miehling**[1], **Xiaojuan Zhou**[2], **Simonas Masiulis**[1,4], **Steven W. Hardwick**[5], **Dimitri Y. Chirgadze**[5], **Keith W. Miller**[2,*], **A. Radu Aricescu**[1,*]

[1]MRC Laboratory of Molecular Biology, Francis Crick Avenue, Cambridge, CB2 0QH, UK

[2]Department of Anesthesia, Critical Care and Pain Medicine, Massachusetts General Hospital, Harvard Medical School, Boston, MA, USA

[3]Division of Structural Biology, Wellcome Centre for Human Genetics, University of Oxford, Roosevelt Drive, Oxford, OX3 7BN, UK

[5]Department of Biochemistry, University of Cambridge, Tennis Court Road, Cambridge, CB2 1GA, UK

Abstract

Type-A γ-aminobutyric acid receptors ($GABA_AR$s) are pentameric ligand-gated chloride channels that mediate fast inhibitory signalling in neural circuits [1,2] and are modulated by essential medicines including general anaesthetics and benzodiazepines [3]. Human $GABA_AR$ subunits are encoded by 19 paralogous genes which can, in theory, give rise to 495,235 receptor types. Yet, the principles governing the formation of pentamers, the permutational landscape of receptors that may emerge from a subunit set and the impact this has on GABA-ergic signalling remain largely unknown. Here, we use cryogenic electron microscopy (cryo-EM) to determine structures of extrasynaptic $GABA_AR$ assembled from α4, β3 and δ subunits, and their counterparts incorporating γ2 instead of δ subunits. In each case we could identify two receptor subtypes with distinct stoichiometries and arrangements, all four differing from those previously observed for synaptic, α1-containing receptors [4–7]. This, in turn, affects receptor responses to physiological

[*]Correspondence to: asente@mrc-lmb.cam.ac.uk or k_miller@helix.mgh.harvard.edu or radu@mrc-lmb.cam.ac.uk .
[4]Current address: Materials and Structural Analysis Division, Thermo Fisher Scientific, Achtseweg Noord, Eindhoven, 5651 GG, Netherlands

Author Contributions
AS, KWM and ARA conceived the project. AS generated the α4β3γ2 cell pool and YJ generated the α4β3δ cell lines. AS and SM purified proteins and prepared cryo-EM samples. AS, SWH and DYC collected cryo-EM data. AS, KN and SM processed cryo-EM data. AS, TM, JM and ARA built and refined atomic models. RD and KWM designed, performed and analysed electrophysiology experiments. XZ and KWM designed, performed and analysed radioligand binding assays. AS designed and performed bioinformatics analyses. AS and KN designed, performed and analysed simulations of receptor assembly. AS, KN, RD, KWM and ARA wrote the manuscript, with input from all authors.

Competing interest statement
The authors declare no competing interests.

Peer review information Nature thanks ….for their contribution to the peer review of this work.

Biological materials availability
Cell lines, cell pools and cDNA constructs generated for the purpose of this study are available from ARA upon reasonable request.

and synthetic modulators by creating or eliminating ligand binding sites at subunit interfaces. We provide structural and functional evidence that selected $GABA_AR$ arrangements can act as coincidence detectors, simultaneously responding to two neurotransmitters, GABA and histamine. Using assembly simulations and single-cell RNA sequencing data [8,9], we calculate upper bounds for receptor diversity in recombinant systems and *in vivo*. We propose that differential assembly is a pervasive mechanism for regulating the physiology and pharmacology of $GABA_AR$s.

Human $GABA_AR$s assemble from a pool of nineteen subunits (α1-6, β1-3, γ1-3, δ,, 1-3 and) with cell-type specific expression patterns [1,2,10]. Their homo- and hetero-pentameric combinations give rise to receptors with different localization and functions [1,2,10–14]. For example, in the central nervous system, receptors containing the γ subunit localize both synaptically and extrasynaptically, bind GABA with lower affinity and desensitize more rapidly than δ subunit-containing receptors [14,15]. In contrast, in the predominantly extrasynaptic δ-containing receptors, GABA binds with higher affinity and has lower efficacy than in the γ-containing receptors [14].

The stoichiometry and arrangement of subunits in a pentamer are fundamental determinants of receptor signalling because interfaces between subunits harbour binding sites for agonists, antagonists and allosteric modulators. Therefore, different subunit arrangements within a receptor pentamer can result in the emergence or disappearance of ligand binding sites [16]. Synaptic $GABA_AR$s are thought to assemble into pentamers with invariant arrangements and stoichiometry (βαγβα, counter clockwise), which is supported by cryo-EM structures of receptors containing the α1, β1-3 and γ2 subunits, including human α1β3γ2 bound to the Ro15-4513 benzodiazepine reported here (Fig. 1a) [4–7]. However, the arrangements and stoichiometries of extrasynaptic receptors, and of synaptic receptors assembled from different subunit pools, are uncertain [17–21]. Moreover, the overall landscape of possible receptor subtypes and the extent to which they can diversify $GABA_AR$ physiology and pharmacology remain unknown. Given the plethora of pharmacological agents with anticonvulsant, anti-anxiety, analgesic, sedative and anaesthetic properties that target $GABA_AR$s [3], mechanistic insights into the interplay between stoichiometry and function are important not only to better understand GABA-ergic signalling, but also to provide new avenues for drug development.

Structural evidence for $GABA_AR$ heterogeneity

To explore the diversity of possible receptor subtypes, we first sought to solve the structure of human α4β3δ, an extrasynaptic $GABA_AR$. Previous work has suggested that, when co-expressed, these subunits form multiple receptor populations depending on transfection ratios and expression systems [19,20,22]. Thus, we generated two mammalian cell lines by varying the relative amounts of cDNA encoding individual subunits (Methods).

Unexpectedly, identical α4β3δ $GABA_AR$ structures were solved from both cell lines (Fig. 1b, Extended Data Fig. 1a, c, e and Supplementary Fig. 1). These structures revealed that the receptor contains one α4, three β3 and one δ subunit, in a βαδββ arrangement. From the same samples, we classified a second population of receptors, the di-heteromeric β3δ subtype containing four β3 and one δ subunit (Fig. 1c and Extended Data Fig. 1b,

d). While the α4β3δ $GABA_AR$ contains a single putative GABA binding site at the $\beta3^+/\alpha4^-$ interface, it also harbours two putative histamine-binding pockets at the $\beta3^+/\beta3^-$ interfaces (principal and complementary faces of the interface are denoted as (+) and (-), respectively) [23,24]. Therefore, both neurotransmitters could bind these receptors. In contrast, a prototypical synaptic receptor, such as α1β3γ2 (arranged as βαγβα), has GABA-binding pockets at its two $\beta3^+/\alpha1^-$ interfaces but no known binding sites for histamine, as the pentameric arrangement of subunits does not present a $\beta3^+/\beta3^-$ interface (Fig. 1a) [6,7]. On the other hand, the β3δ subtype has putative histamine-binding pockets at the three $\beta3^+/\beta3^-$ interfaces.

To investigate whether the stoichiometry observed in the α4β3δ $GABA_AR$ is driven by the δ subunit, we solved the structure of the α4β3γ2 receptor (Fig. 1d and Extended Data Fig. 1f). To our surprise, we found yet another subunit arrangement compatible with a GABA/histamine "crosstalk", albeit different to the one observed in α4β3δ receptors. The α4β3γ2 assembly contains one α4, one γ2 and three β3 subunits, arranged as ββγβα, which harbours putative binding sites for GABA and histamine at the $\beta3^+/\alpha4^-$ and $\beta3^+/\beta3^-$ interfaces, respectively (Extended Data Fig. 2c). From the same dataset, we could also solve the structure of a β3γ2 subtype (Fig. 1e and Extended Data Fig. 1g). In contrast to the β3δ receptor, β3γ2 incorporates two γ2 subunits at non-adjacent positions, in agreement with previous stoichiometry estimates for the β2γ2 receptor [25]. Importantly, both the β2γ2 and β3γ2 subtypes have been shown to form functional, GABA-gated channels [25,26]. Interestingly, we did not observe receptors with the same subunit composition but different stoichiometries, such as β3δ with two non-adjacent δ subunits or β3γ2 with a single γ2 subunit. Therefore, we conclude that cells expressing α4, β3, δ or α4, β3, γ2 subunits assemble multiple receptor populations in a differential (i.e., context-dependent) but non-random manner.

Differential assembly diversifies signalling

To examine whether and how the observed subunit arrangements may diversify receptor function, we focused on the putative GABA/histamine interplay at the α4β3δ receptor. Histamine modulation has previously been observed for several $GABA_AR$ subtypes, including the α1β2γ2 [24], α1β3δ, α4β3γ2 and α4β3δ [27]. The joint presence of α4 and β3 subunits showed the strongest enhancement of GABA currents and an allosteric mechanism for histamine action was proposed [27]. We solved the structure of the α4β3δ receptor (βαδββ arrangement) simultaneously bound to both ligands (Fig. 2a–c and Extended Data Fig. 1c). The $\beta3^+/\alpha4^-$ agonist pocket is occupied by a GABA molecule while the equivalent pockets at the two $\beta3^+/\beta3^-$ interfaces bind histamine (Fig. 2a–c and Extended Data Figs. 2–3). All three pockets adopt compact conformations, with loops-C closed and ligands coordinated in each corresponding 'aromatic cage' (Extended Data Fig. 3 and Supplementary Fig. 2). Although a low-affinity GABA-binding site has previously been proposed at the $\beta3^+/\delta^-$ interface [28], we do not observe any ligand density in this pocket, which is supported by our electrophysiological recordings (Extended Data Fig. 4a–c). The ion channel is desensitised, as previously described for synaptic and homomeric β3 receptors [6,7,23,29]. From the same dataset, we classified a subpopulation of α4β3δ subtype (βαδββ) where all three pockets mentioned above are occupied by histamine

molecules (Extended Data Figs. 1e, 2b, 3 and Supplementary Fig. 2). Although in this case the extracellular domain (ECD) adopts an activated conformation, the ion channel is closed, illustrating a pre-open "flip" state consistent with the partial agonism of histamine at receptors containing $\beta3^{+}/\beta3^{-}$ interfaces (Extended Data Fig. 2f) [30]. Moreover, the same dataset also contains β3δ subtype, devoid of α4 subunits and thus unable to bind GABA (Extended Data Figs. 1d, 2b and 4b). In this map, histamine molecules occupy the agonist pockets at the three $\beta3^{+}/\beta3^{-}$ interfaces, and the ion channel is desensitised (Extended Data Fig. 2f). In the context of a heterogeneous $GABA_AR$ population, the relative concentration of agonists and their binding properties will ultimately determine the identity of ligands occupying individual pockets and their signalling impact.

We investigated the functional consequences of GABA and histamine crosstalk at the 4 3 receptor by performing whole-cell patch clamp electrophysiology on the cell line used for structural analysis. Both GABA (EC50 70 nM) and histamine (EC50 835 μM) are agonists, with the latter being 3-fold more efficacious. (Fig. 2d and Extended Data Fig. 4d–f), consistent with previous studies in 4 3 and 4 3 2 receptors [27]. Co-application of these ligands results in a cumulative enhancement of current amplitude (Fig. 2d and Extended Data Fig 4g). However, proving that the observed enhancement is a consequence of GABA and histamine action at the α4β3δ receptors is complicated by the presence of other subtypes that respond to either one of the two ligands (such as the β3δ subtype), as demonstrated by structural studies. One indication of crosstalk at the level of a single α4β3δ receptor is that, in the continuous presence of a low concentration of histamine (100 μM), deactivation of currents following a brief pulse of 10 μM GABA is accelerated (Figure 2e–f). A decrease in peak current amplitude is also observed under these experimental conditions (Figure 2e–f, Extended Data Fig. 4h–k).

To further deconvolve responses from different receptor subtypes present in the same cell, we first established that GABA at 100 nM robustly activates currents in α4β3δ cells, barely in α4β3 and not in β3 or β3δ cells (Extended Data Fig. 5a–d). Similarly, histamine (300 μM) robustly enhances GABA currents only in α4β3δ cells. Only modest responses to co-application of 100 nM GABA and 300 μM histamine are observed in α4β3, β3δ and β3 cells, attributable to histamine currents alone (Extended Data Fig. 5e). Taken together, our results indicate that histamine has dual and opposing actions on α4β3δ receptors—it is an agonist itself, and it also accelerates closure of GABA-activated receptors. Thus, differential assembly of $GABA_ARs$ in a single cell diversifies signaling by enabling activation and/or modulation of receptor ensembles by multiple neurotransmitters, such as GABA and histamine. The timing, order, strength and duration of neurotransmitter exposure can affect the signaling outcome through 4 3 receptors and the overall output of each cell is a summed response of all receptor subtypes that respond to the particular ligands.

Differential assembly affects drug responses

The binding and functional impact of synthetic $GABA_AR$ modulators may also be altered by combinatorial expression of subunits and their assembly permutations and result in off-target effects or complete loss of ligand activity. We illustrate this phenomenon with two drug candidate molecules, THIP (4,5,6,7-tetrahydroisoxazolo[5,4-c]pyridin-3-ol, also known as

gaboxadol), a synthetic agonist of α4β3δ receptors recently investigated as a treatment for insomnia [15,31,32], and Ro15-4513, a partial inverse agonist benzodiazepine thought to bind both γ- and δ-containing receptors (e.g., α1β3γ2 and α4β3δ) [33,34]. Ro15-4513 was reported to reverse low-dose alcohol potentiation of $GABA_A$Rs, and thus ethanol inebriation, by acting specifically on extrasynaptic α4/6β3δ subtypes (also dubbed the "one glass of wine" receptors [35]), although these findings have been challenged [36].

We solved the structure of α4β3δ(βαδββ) bound to THIP and histamine (Extended Data Fig. 1h). In agreement with our GABA+histamine structure and previous work [37], we found THIP bound in the $\beta3^+/\alpha4^-$ agonist pocket, and histamine at the two $\beta3^+/\beta3^-$ interfaces (Fig. 3a and Extended Data Figs. 2d, 3 and Supplementary Fig. 2). We also found THIP density in the equivalent pocket at the δ^+/β^- interface (Fig. 3b), consistent with previous studies [28]. Binding of this agonist to two distinct sites provides a structural explanation for previous observations that THIP has higher potency and supramaximal efficacy at α4β3δ relative to other receptors subtypes [37,38]. Furthermore, from the same dataset we also solved the structure of a β3δ receptor (Extended Data Fig. 1i). Here, histamine occupies the agonist sites at the three $\beta3^+/\beta3^-$ interfaces while THIP binds only the δ^+/β^- pocket. These observations directly illustrate why functional measurements for THIP (or any molecule active at $GABA_A$Rs) represent an integrated response of all receptor subtypes present and capable of binding that compound, and that targeting a specific receptor arrangement with unique ligand-binding sites might yield drugs with better specificity and fewer side effects [39].

To investigate the mechanism of Ro15-4513 action as an alcohol antagonist, we first explored its interaction with the α1β3γ2 receptor (βαγβα, Extended Data Fig. 1j). The ligand unambiguously occupies the $\alpha1^+/\gamma2^-$ benzodiazepine pocket in the ECD (Fig. 3c and Supplementary Fig. 2). Surprisingly, attempts to solve the structure of α4β3δ bound to Ro15-4513 did not reveal any density for the drug. Radioligand binding assays confirmed that Ro15-4513 binds membranes from α1β3γ2 cell line as well as α4β3γ2 cell pool, but not those from α4β3δ or α4β3 cell lines (Fig. 3d). Furthermore, whole-cell electrophysiology recordings demonstrate that Ro15-4513 has little effect on GABA currents in the α4β3δ cell line (Supplementary Fig. 3). For the α4β3γ2 cell pool, it remains unclear if Ro15-4513 binds to a non-canonical interface (e.g., the $\beta3^+/\gamma2^-$) or whether receptor subtypes containing an $\alpha4^+/\gamma2^-$ interface may also be present. The superposition of $\alpha1^+/\gamma2^-$ and $\alpha4^+/\delta^-$ pockets shows that, among multiple potentially clashing residues, H92 on the δ^- side of the interface would prevent binding of Ro15-4513 in the mode seen in α1β3γ2 (Extended Data Fig. 6a–d). The structural similarity of Ro15-4513 to all other imidazo-benzodiazepines, and prior knowledge that "classical" benzodiazepines do not bind α4 and α6-containing receptors due to the presence of R135 ($\alpha4^+$ numbering) [7,40], help rationalize why most (if not all) benzodiazepines do not bind the $\alpha4^+/\delta^-$ and, by extension, $\alpha6^+/\delta^-$ ECD interfaces. Therefore, the identity of subunits and their particular arrangement within pentameric receptors dictate the binding and functional effects of both physiological and synthetic ligands.

Estimation of $GABA_AR$ diversity

Prompted by the observation that a cell line expressing three $GABA_AR$ subunit genes gives rise to at least two distinct receptor arrangements, we sought to investigate the possible subtype diversity in the brain. Because cryo-EM reconstructions are biased, i.e. limited to particles one can purify and classify, it is possible that the receptor heterogeneity in engineered cell lines, as well as in $GABA_AR$-expressing neurons, might be even greater. We analysed single-cell RNA sequencing (sc-RNAseq) data from human cortex [8,9] and found that mRNAs of up to 14 different $GABA_AR$ subunits can be simultaneously present in individual cell types (Extended Data Fig. 7a–b and Methods). While we acknowledge that mRNA abundance may not be a reliable predictor of protein levels, the specific pattern of 14 co-expressed subunits observed in the cortex can theoretically produce up to 62,847 distinct receptor subtypes (Supplementary Methods and Supplementary Table 1).

To overcome current cryo-EM limitations and estimate the potential for $GABA_AR$ diversity, we simulated the equilibrium distribution of pentameric receptors assembled from a pool of three distinct monomeric subunits, denoted as α, β and δ/γ (Fig. 4a, Methods and Supplementary Discussion). With the simulation, we seek to calculate the distribution of receptor subtypes given two sets of parameters: subunit abundances and relative interface likelihoods. We simulate the distributions over a large range of relative subunit abundance and interface likelihoods and search for mutually consistent conditions that mimic the experimentally observed subtype distributions (Methods and Supplementary Discussion). In such conditions, we consistently find additional receptor subtypes which may exist and contribute to the overall signalling response of a cell (Fig. 4b). For example, αβ heterodimeric receptors represent a major population across many conditions in the α4β3δ simulation, in agreement with previous observations that a large fraction of α4-containing $GABA_A$ receptors isolated from rat brain do not contain γ or δ subunits [41] . Notably, α4β3δ and α4β3γ2 receptors with two α4 subunits are predicted to exist but we are unable to experimentally identify them due to the lack of specific nanobodies for their inter-subunit interfaces. Altogether, the sc-RNAseq data and computational simulations suggest that the diversity of subtypes, in our cell lines and the brain, is likely greater than what we observe by cryo-EM and may also include less abundant subtypes with distinct signalling properties.

Discussion

It has been recognised in the past that co-expression of multiple $GABA_AR$ paralogue genes could increase the diversity of receptor subtypes and responses to GABA [42] . Our study provides a direct, structural demonstration that differential $GABA_AR$ assembly gives rise to an ensemble of receptors with distinct signalling properties. Several lines of evidence support the hypothesis that similar diversity occurs *in vivo*. For example, three distinct populations of extrasynaptic receptors were identified based on conductance measured by single-channel electrophysiology in cerebellar granule cells [43] . Multiple receptor subtypes were also observed by native pulldowns with subunit-specific antibodies [44] or by immunofluorescence [45,46] . More recently, cerebellar granule cells were found to assemble distinct populations of 1 6 2 receptors, in which either the 1 or α6 subunit is at the principal side of the α^+/γ^- interface [16] . Structures of native receptors and a detailed characterisation

of assembly pathways are needed for a more complete understanding of the $GABA_AR$ signalling pathways. The potential physiological implications of simultaneous GABA and histamine binding to $GABA_ARs$ are discussed in Supplementary Information section 1.2.

Our simulations and analysis of sc-RNAseq data suggest that, by controlling relative subunit abundance and by modulating interface affinities, perhaps through assembly factors or chaperones, it is possible to generate a large ensemble of receptors. Because these parameters are regulated *in vivo*, differential assembly of $GABA_ARs$ may be a mechanism to rapidly adapt cellular responses to specific signalling needs by enabling diversification of input recognition and enhanced capacity to finely tune the summed output [39] . Individual neurons or synapses may also assemble distinct receptor subtypes across spatial locations, developmental stages, and physiological or disease states [47–50] . Such flexibility may have enabled the establishment of intricate developmental programs and facilitated the evolution of complex neuronal circuits and behaviours in animals.

Methods

Protein production and purification

Generation of the α4β3δ cell lines—Stable tetracycline-inducible HEK293S TetR [54] cell lines expressing full-length human 4, 3 and δ subunits under antibiotic selection (zeocin, hygromycin and geneticin/G418, respectively) were prepared as described previously [21] . The δ subunit was modified to include an N-terminal FLAG tag and a C-terminal linker (GGS)3GK followed by the 1D4 tag (TETSQVAPA). To investigate stoichiometric variability of 4 3δ $GABA_ARs$, we generated two stable cell lines using different transfection ratios. One cell line was transfected with molar ratios of α4:β3:δ=2:1:0.25, predicted to yield receptors with subunit composition of two α4, two β3 and one δ subunit [19] . The other cell line was transfected with about three times less β3 subunit relative to the first one (α4:β3:δ=2:0.3:0.25 molar ratios), to minimise β3 homo-oligomerisation.

α4β3δ protein production—Suspension cultures were grown at 37°C, 160 r.p.m., 8% CO_2, in FreeStyle 293 expression medium (Gibco), supplemented with 1% fetal bovine serum (Invitrogen), 1% L-Glutamine, 1% non-essential amino acids and antibiotics: 200 μg/ml geneticin, 50 μg/ml hygromycin-B, 250 μg/ml zeocin, 5 μg/ml blasticidin and 10,000 units/ml penicillin/streptomycin (zeocin, hygromycin and blasticidin from Thermo Fisher Scientific, Pen/Strep mix prepared in house). Once cell density reached 2.5×10^6 ml^{-1}, expression was induced with 2 μg/ml doxycycline (Sigma) in the presence of 5 mM sodium butyrate and 1 mg/l I -mannosidase inhibitor kifunensine (Toronto Research Chemicals). After 24 h, cells were collected by centrifugation at 4000 r.p.m. and snap-frozen in liquid nitrogen.

Generation of the α4β3γ2 cell lines and protein production—Full-length human γ2L subunit codon-optimised for expression in human cells was cloned into the pHR vector [55] . A $(GGS)_3GK$ linker followed by the 1D4 tag was added to the C-terminus of the γ2L subunit for purification purposes. Lentiviral particles containing the γ2L subunit cDNA were prepared as previously described [55] , and used to infect a stable, tetracycline-inducible HEK293S TetR cell line expressing full-length human 4 and 3 under antibiotic

selection (zeocin and hygromycin, respectively) [21] . Protein production in suspension cultures proceeded as described above for the 4 3δ cell lines.

Production of the α1β3γ2 receptor—The cell line and protocols used to produce the α1β3γ2 receptor were previously published [56,6,7] .

$GABA_A$ receptor purification and nanodisc reconstitution—Frozen cell pellets were resuspended on ice in buffer A (50 mM HEPES pH 7.5, 300 mM NaCl) supplemented with 1% (v/v) mammalian protease inhibitor cocktail (Sigma-Aldrich). Cells were lysed by 1% (w/v) Lauryl Maltose Neopentyl Glycol (LMNG, Anatrace) for 1 h at 4°C then centrifuged for 30 min at 10,000g (4°C) [6] . The supernatant was incubated with 1D4 affinity resin rotating slowly for 1 h at 4°C [29] . The 1D4 affinity resin was generated in house using the anti-Rho-1D4 antibody from the University of British Columbia. The resin was recovered by centrifugation (500*g*, 5 min) then washed with buffer B (buffer A supplemented with 0.1% (w/v) LMNG). For the α4β3δ/β3δ + HEPES and α4β3δ/β3δ + histamine + GABA samples, the wash buffer also contained 0.01% BBE (w/v). While attached to 1D4 resin, receptors were incubated with phosphatidylcholine (POPC, Avanti) and bovine brain lipid (BBL) extract (type I, Folch fraction I, Sigma-Aldrich) mixture (POPC:BBL = 85:15) for 30 min at 4°C. Excess lipids were removed by pipetting after allowing the beads to settle, then samples were mixed with 100 μl (5 mg/ml) of MSP 2N2 and incubated for 30 min at 4°C [7] . The detergent was removed by incubating the resin with 20 mg Biobeads for 90 min at 4°C, followed by washing with 20-30 bed volumes of buffer A. Receptor samples were eluted with buffer C (12.5 mM HEPES pH 7.5, 125 mM NaCl) supplemented with 2 mg/ml 1D4 peptide (TETSQVAPA).

Cryo-EM sample preparation

Prior to freezing, all samples were deglycosylated with Endoglycosidase F1 (1% v/v) for 1 h at room temperature. Samples were incubated for 30 min with 5 μM Nb25 [57] and 1.7 μM Mb192 [58] to facilitate particle alignment and improve orientation distribution, respectively. During this incubation, ligands were also added at the following concentrations: 0.2 mM GABA, 1 mM histamine, 1 mM THIP, and 10 μM Ro15-4513, for the respective samples. A 3.5 μl volume of sample was applied to glow-discharged (PELCO easiGlow, 30 mA for 30 s) gold R1.2/1.3300 mesh UltraAuFoil grids [59] (Quantifoil) and incubated between 0-30 s at 14°C. The excess liquid was blotted for 4.0-4.5 s prior to plunge-freezing into liquid ethane using a Leica EM GP2 plunger (Leica Microsystems; 95% humidity, 14 °C). Grids were stored in liquid nitrogen prior to data collection.

Cryo-EM data collection

Cryo-EM datasets were collected on Titan Krios G3 microscopes at the MRC LMB or the Department of Biochemistry EM facility (BiocEM, University of Cambridge) in electron counting mode at 300 kV. Both microscopes were equipped with Gatan K3 cameras and Gatan BioQuantum energy filters. Before data acquisition, two-fold astigmatism was corrected and beam tilt was adjusted to the coma-free axis using the autoCTF function (EPU v2.00-2.11, Thermo Fisher Scientific). All datasets were acquired automatically using EPU

software (Thermo Fisher Scientific, version 2.0-2.11). Detailed data acquisition parameters for all datasets are given in Extended Data Table 1.

Cryo-EM image processing

A typical image processing pipeline is shown in Extended Data Figure 8. Gain-uncorrected K3 super-resolution movies in TIFF format were motion- and gain-corrected using RELION's implementation of the MotionCor2 algorithm [60], with frames grouped to yield a total fluence corresponding to ~1 $e^-/Å^2$ per frame and binned by 2. Contrast transfer function (CTF) estimation was performed with CTFFIND-4.1.13 [61] using the sums of power spectra from combined fractions corresponding to an accumulated fluence of 4 $e^-/Å^2$. Micrographs whose estimated resolution from CTFFIND was worse than 5 Å were removed. Particles were picked using a re-trained BoxNet2D neural network in Warp v 1.0.7 [62] then re-extracted in RELION with a pixel size ~1.1 Å and $(246\ pix)^2$ box size. All initial data cleaning procedures were performed in cryoSPARC (from v2.15 to 3.2.0) [63]. First, particles were imported into cryoSPARC and subjected to 2D classification, then good classes were selected to generate an ab-initio model using stochastic gradient descent with at least two seeds. After homogeneously refining the ab-initio model, all picked particles were included in one or more rounds of heterogeneous refinement in cryoSPARC using three or more classes and the refined model as reference. Aiming to retain as many particles as possible, only particles belonging to classes displaying features of structural damage (e.g., incomplete ECD/TMD or collapsed TMD) were excluded and the rest were converted into STAR format using csparc2star from UCSF PyEM v0.5 suite [64]. Particles were then re-imported into RELION v3.1 [65,66] for a standard 3D auto-refinement. Refined maps were visually inspected and an optional 3D classification step without alignment was performed if the maps displayed structural damage features. Particles belonging to the best class were re-refined, followed by three steps of CTF refinement: first refining magnification anisotropy; then refining optical aberrations (up to the 4th order); and finally refining per-particle defocus [67]. Next, 3D-auto-refinement was performed, followed by Bayesian polishing to optimise per-particle beam-induced motion tracks [68], and another round of auto-refinement. During the polishing step, target particle box size was ~$(270\ Å)^2$. CTF refinement was then repeated for optical aberration correction, magnification anisotropy, per-particle defocus and per-micrograph astigmatism, followed by auto-refinement. For the highest resolution α4β3δ/β3δ dataset (+HEPES), additional steps at this stage included a second round of Bayesian polishing with trained parameters, auto-refinement, CTF refinement as in previous step, followed by auto-refinement. To separate α4β3δ and β3δreceptors, a soft mask surrounding only the Nb25 at all five possible symmetry-related positions was created by simulating Nb25 density from a previously published model (PDB ID: 7A5V) with UCSF Chimera v1.0 [69] molmap function, and low-pass filtered to 15 Å. To separate α4β3γ2L and β3γ2L receptors, a soft mask surrounding only the vestibule glycan and vestibule-lining protein residues was created by simulating density from a previously published model (PDB ID: 6HUG) with UCSF Chimera molmap function, which was then low-pass filtered to 15 Å. These masks were used during 3D classification without alignment and regularization parameter T=32 or T=64. In some instances, classification on Nb25 alone did not provide sufficient separation of α4β3δ and β3δ particles. To overcome this, we focused the classification simultaneously on the vestibule glycan of the α4 subunit and

the N80 glycan of the β3 subunit, with T=128. After selecting classes corresponding to α4β3δ,β3δ, α4β3γ2L or β3γ2L receptors, a final round of 3D auto-refinement with local signal-to-noise filtering using SIDESPLITTER [70] implemented in RELION was followed by standard post-processing procedures in RELION. Local resolution plots were generated with Resmap (version 1.1.4) [71] . Orientation distributions were analysed by cryoEF v1.2 [72] . Renderings of maps and models were done in ChimeraX-1.1.1 [73] or PyMOL v1.8.4.

Atomic model building and refinement

The initial models used were PDB IDs 7A5V (for the β3 subunit) [23] and 6HUG (for α1 and γ2 subunits) [7] . Starting models for the α4 and δ subunits were generated in SWISS-MODEL [74] . Restrains for small molecules were generated by the Grade webserver (Global Phasing Ltd.) using SMILES strings [75] from ChemDraw JS v2.0.0.9 (PerkinElmer). Iterative rounds of model building and refinement were performed in Coot v0.9.4 [76] , REFMAC v5.8.0258 [51] and Phenix v1.19.2 [53] . Secondary structure restraints from ProSMART v0.859 were used during the initial stages of refinement [77] . Models were validated using MolProbity v4.2 [52] . Model building and refinement parameters and statistics are provided in Extended Data Table 2.

Electrophysiology

Electrophysiology measurements were performed on the 4 3 cell line described above (4 3N-Flag-C-L3-1D4, subunit cDNA transfection ratio α4:β3:δ=2:0.3:0.25), an 4 3 cell line [21] , and a 3 cell line (Supplementary Methods) transiently transfected with N-Flag-δ-C-L3-1D4 pCMV as indicated in the figures. Cells were seeded on glass coverslips and $GABA_A$ gene expression was induced with tetracycline (2 μg/ml) for 28–32h. $GABA_A$ receptor mediated chloride currents were recorded using whole-cell patch-clamp electrophysiology at room temperature (20–22°C). The recording chamber was continuously perfused with the bath solution (in mM): 145 NaCl, 5 KCl, 10 HEPES, 2 $CaCl_2$, 1 $MgCl_2$ and 10 glucose, pH 7.4 (pH adjusted with NaOH). The pipette solution for whole-cell recordings contained (in mM) 140 KCl, 10 HEPES, 1 EGTA and 2 $MgCl_2$, and 2 Mg-ATP at pH 7.3 (pH adjusted with KOH). Open pipette resistances ranged from 2 to 2.3 MΩ. Series resistance ranged from 0.5 to 2.8 MΩ and was monitored before and after recordings. Cells whose series resistances changed by 10% or more during recordings were not analyzed. Cell capacitances ranged from 4 to 16 pF. The membrane capacitance and series resistance were compensated electronically by > 85% with a lag of 10 μs. Cells were voltage clamped at –50 mV using a patch clamp amplifier (Axopatch 200A or Axopatch 200B, Molecular Devices Corp., Sunnyvale, CA, USA). $GABA_A$Rs were activated with agonists delivered via a quad-channel superfusion pipette coupled to a piezoelectric element that switched the superfusion solution in <1ms [78] . Cells were washed with bath solution alone for at least 1 min between each pulse of agonist application to allow the receptors to recover from desensitization. In some cases, more than one pulse was delivered 1 min apart and the traces acquired were averaged for analysis. Data were manually leak subtracted before analysis and low-pass filtered offline with a Gaussian filter at 250 Hz for presentation.

The GABA EC50 was determined by exposing the cells to three 8s pulses: (1) 10 mM GABA; (2) varying concentrations of GABA (1 nM-10 μM), and (3) 10 mM GABA. Peak

current amplitudes obtained with the second pulse were normalized to the average peak amplitudes obtained in the first and third pulses. The histamine EC50 was determined by a two-pulse protocol; (1) a 4s pulse of various concentrations of histamine (0.03 – 10 mM), and (2) a 1s pulse of 10 mM GABA. Peak current amplitudes obtained in the first pulse were normalized to those obtained in the second pulse. All experimental pulses were separated by a 6s wash.

GABA and histamine efficacy were determined in whole cell configuration using a two-pulse protocol. The first pulse was 2 s of either GABA (10 mM), histamine (10 mM) or equimolar GABA + histamine (10 mM). After a wash of 6 s, the second pulse was 1 s of 10 mM GABA + 30 μM etomidate, assumed to open the maximum number of receptors. Current traces shown in Fig. 2d and peak amplitudes were normalized to the peak amplitude of this second pulse. Current deactivation was studied in the whole-cell configuration because the receptor amounts were too low for measurable currents in outside-out macro patches. Unlike GABA, histamine gates 4 3 receptors in the same concentration range as 3 receptors (Extended Data Fig. 4d–e) [21,24,28] . Therefore, we utilized the specificity of GABA in the 1-10 μM range to selectively gate 4 3 receptors. A small fraction of the 3 and 4 3 (if present) may be activated by 10 μM GABA [28] . Low concentration of histamine (100 μM) was used to modulate the gating equilibrium. Deactivating currents were elicited from the same cell by a 200 ms pulse of 10 μM GABA alone and data was acquired for 5s. For each cell the three traces separated by 60s washes were: (1) GABA alone; (2) histamine (100 μM) present for 60 s before the GABA pulse and present throughout deactivation, and (3) GABA alone. Current traces were normalized to their own peak amplitudes for better visual comparison of deactivation rates shown in Fig. 2f.

Electrophysiology data acquisition and analysis

Electrophysiology data were acquired using Clampex version 8.1 (Molecular Devices), digitized at 5kHz or 10 kHz depending upon the length of the pulse. Data were low pass filtered at either 5kHz or 10 kHz. Deactivating phases of the currents were fit with a one- or two-term exponential equation, as determined by an F-test, using the Levenberg Marquardt algorithm in Clampfit 9.0 (Molecular Devices). The low relative amplitude of the fast phase of deactivation means that its fitted parameters are less accurate than those of the slow phase. Statistical analysis was done using Prism 6 (GraphPad Software). Concentration–response curves were fitted to a Hill equation in the following form:

$$I_{norm} = \frac{1}{1 + 10^{\wedge}((logEC50 - X) * \ Hill\ Slope)}$$

where I_{norm} is the normalized peak current amplitude in the presence of the agonist and the EC50 is the agonist concentration that gives a response halfway to the maximum. Figures were prepared in Origin 6 (OriginLab).

Radioactive ligand binding assays

Radioactive ligand binding assays were carried out as previously described [56] .

Simulations of receptor subtype distributions

Here we describe the implementation details of the simulations for the particular case of three subunits as used in the manuscript. For the general case description of the computational method for simulating the subtype distribution, simulation aims, assumptions, limitations and alternative models of assembly please refer to the Supplementary Discussion section 1.4. Derivation of the equation for calculating the theoretical number of receptor subtypes is also presented in the Supplementary Information.

Model parameters—In the simulation, we define 3 distinct monomeric subunits, arbitrarily denoted as α, β and δ/γ. Two parameter sets are initiated at the start of each run: subunit abundances (an 3-dimensional vector) and affinities (an 3×3 matrix of pairwise affinity coefficients, where [m,n] denotes the relative probability of forming an m^+/n^- interface). The subunit abundance vector is normalised to unit sum of its components.

Computational setup—We iterate over a range of relative subunit abundances and affinity coefficients and simulate M=1000 receptors for each of these cases. We sample a range of relative abundances of any pair of subunits from 1:64 to 64:1 and increase by a factor of 2. Each of the coefficients in the 3×3 affinity matrix loops over a discrete set of values 10^0, 10^1, 10^2, 10^4, 10^5, with the exception of the αα coefficient, which is kept 0. Altogether, we generated a total of 117,100,607 simulated conditions. For every condition, each of the 1000 receptors was assigned to one of the 51 unique subtypes, and the distribution saved together with the parameters that generated it. Custom scripts [79] were written in python v3.6-3.8.

Identification of conditions that favour experimentally observed subtype distributions—To identify simulated conditions that favour subtype distributions observed in our cryo-EM experiments, we searched among all simulated conditions and respective subtype distributions for those that satisfy the following criteria, which are conservatively derived from our cryo-EM observations: (1) of all receptors produced under a given condition, at least 50% incorporate δ (containing the purification tag), (2) of all purifiable receptors (i.e., those from condition (1)), at least 50% are either α4β3δ or β3δ, (3) both α4β3δ and β3δ receptor populations should be abundant and above the noise level, and (4) all other purifiable and solvable receptor subtypes (i.e. those containing the purification tag and the $\beta3^+/\beta3^-$ interface to which the Nb25 nanobody binds) are below the noise level (estimated as $\sqrt{M}$). Because our estimations of the constraints from cryo-EM are imperfect, we confirmed that the general observations are robust to changes in constraint 1 (tested down to 10%). Using analogous constraints, we searched for parameters that favour the receptor distribution observed from the α4β3γ2 cell lines. In addition, given that both of these cell lines express identical α4 and β3 subunit constructs and the cells themselves are identical, we used an additional constraint that all 2×2 pairwise affinity coefficients between these two subunits must be identical between the conditions identified for the α4β3δ and α4β3γ2 cell lines (Supplementary Discussion and Supplementary Fig. 5a). This allowed us to narrow down the range of plausible conditions. All analyses were performed using custom written scripts [79] in R v3.5.2 and RStudio v1.4.1106.

Europe PMC Funders Author Manuscripts

Analysis of $GABA_A$ receptor genes expression

Single-cell RNA-seq data was obtained from Allen Brain Atlas on 25 July 2019 at 13.00 GMT and 18 December 2019 at 23.00 GMT (dataset “Human Multiple Cortical Areas SMART-seq”, download link: https://portal.brain-map.org/atlases-and-data/rnaseq/human-multiple-cortical-areas-smart-seq) [8,9] . Handling of raw data was performed using the rhdf5 2.26.2 R package. For binarized expression data in Extended Data Fig. 7a, a subunit was considered expressed if its precalculated trimmed mean number of counts was greater than zero. Trimmed means are provided by Allen Brain Institute and are generated by first taking the log2 of the summed intron and exon counts of a particular gene across all sequenced cells from a particular cluster (i.e., cell type), then calculating the average number of counts for the middle 50% of the data (i.e., excluding 25% highest and lowest values). Visualization was done using UpsetR package in R. Heatmap of trimmed mean counts was generated using the pheatmap package in R (v1.0.12).

Europe PMC Funders Author Manuscripts

Extended Data

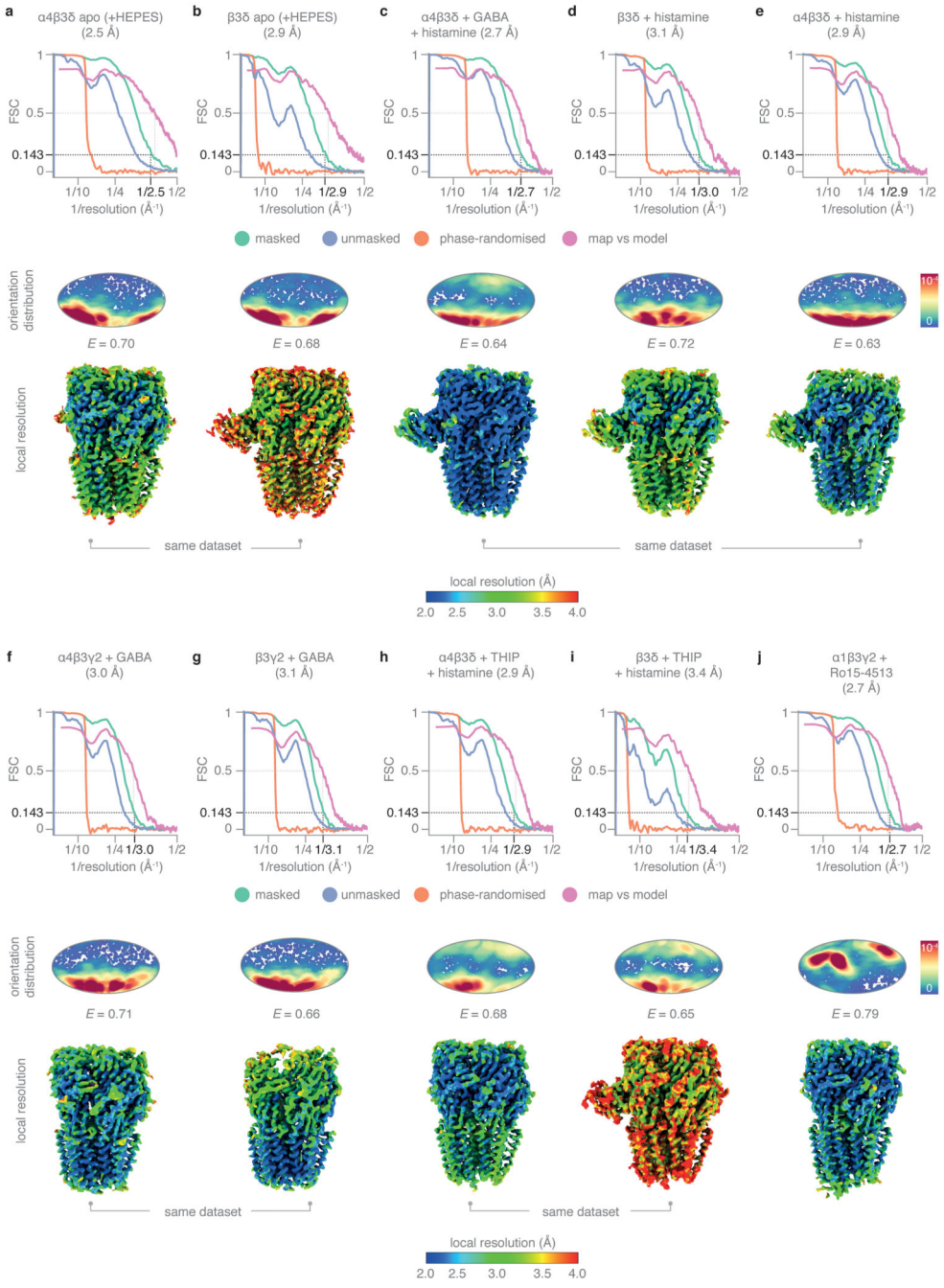

Extended Data Figure 1. Quality of cryo-EM maps and models.

Each panel contains masked, unmasked, phase-randomised and map vs model Fourier shell correlation (FSC) curves (top), particle orientation distribution (middle) and local resolution-coloured maps for each structure. **a, 4 3** "apo" (+HEPES). **b, 3** "apo" (+HEPES). **c, 4 3** + GABA + histamine. **d,** β3δ + histamine. **e, 4 3** + histamine. **f, 4 3 2** + GABA. **g, 3 2** + GABA. **h, 4 3** + THIP + histamine. **i,** 3 + THIP + histamine. **j,** α1β3γ2 + Ro15-4513.

The probability density function for a certain orientation ranges between 0 (blue, low) and 0.0001 (red, high).

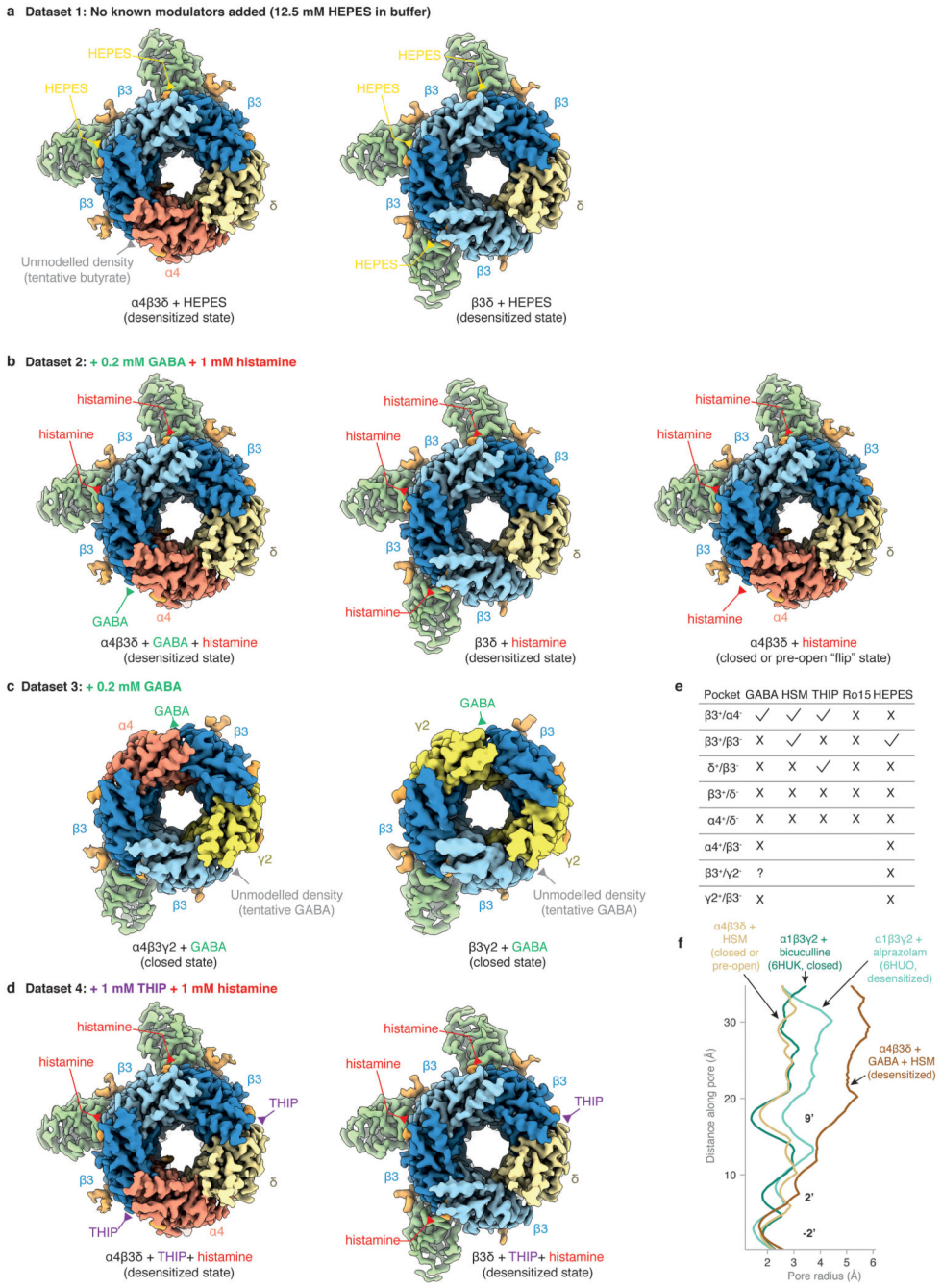

Extended Data Figure 2. Survey of ligands bound in agonist pockets in different datasets.

a, α4β3δ and β3δ $GABA_A$Rs solved in the absence of any known modulators. In both subtypes, HEPES is bound in the $\beta3^+/\beta3^-$ agonist pocket under loop C. **b,** α4β3δ and β3δ $GABA_A$Rs solved in the presence of 0.2 mM GABA and 1 mM histamine. **c,** α4β3γ2 and β3γ2 $GABA_A$Rs solved in the presence of 0.2 mM GABA. **d,** α4β3δ and β3δ $GABA_A$Rs

solved in the presence of 1 mM THIP and 1 mM histamine. **e,** Summary table illustrating ligand vs interface compatibility. Empty spaces are left in cases where insufficient data is available to make a conclusion. For the GABA binding to $\beta3^{+}/\gamma2^{-}$ pocket, a question mark indicates variable occupancy. **f,** Comparison of pore profiles of α4β3δ + GABA + histamine, α4β3δ + histamine, α1β3γ2 + alprazolam (6HUO) and α1β3γ2 + bicuculline (6HUK).

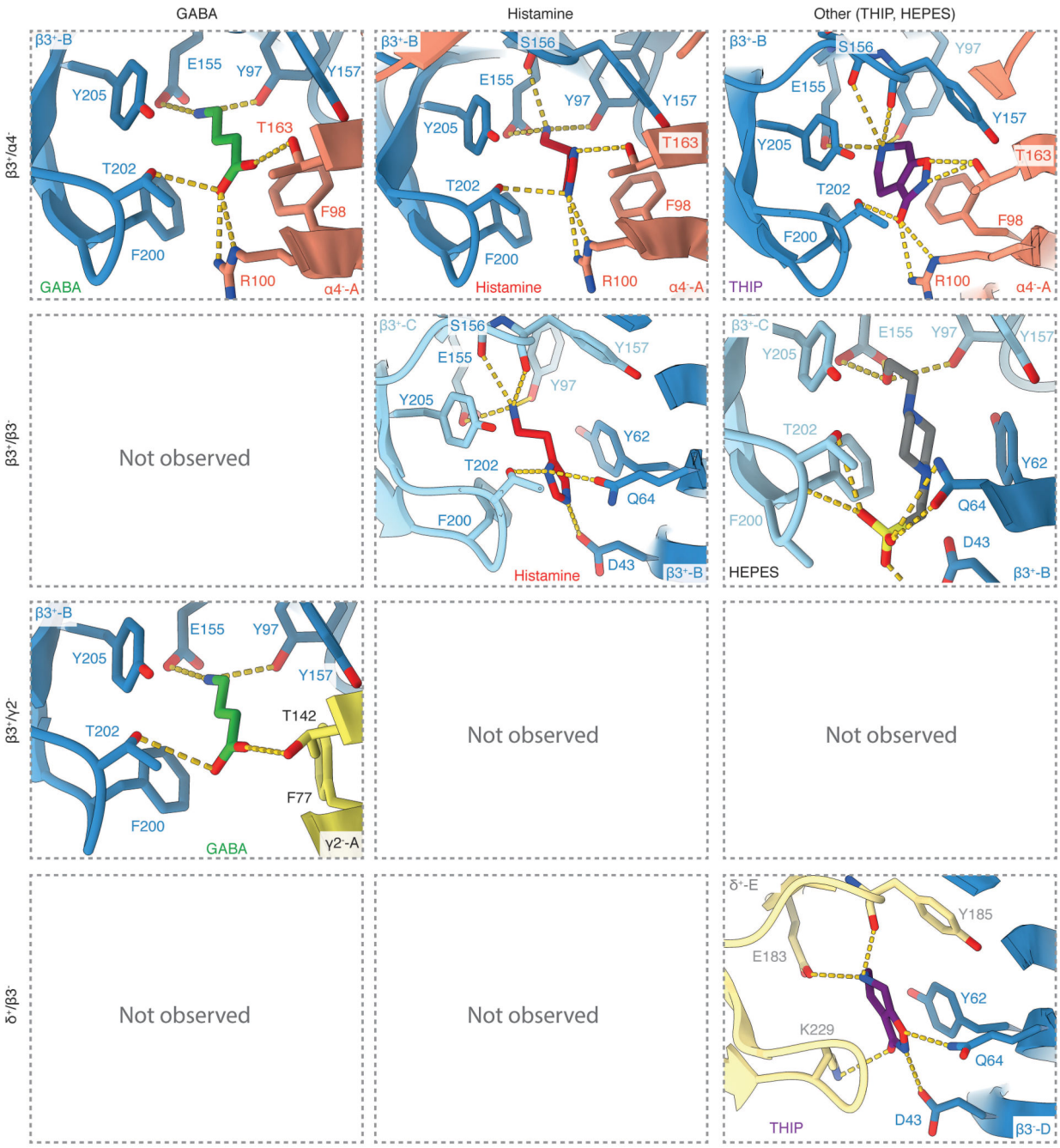

Extended Data Figure 3. Ligand coordination in the "agonist pockets" under the loops C at various inter-subunit interfaces.

All pockets in which a ligand was observed in our structures are shown with a single representative example. Potential hydrogen bonds are displayed as dashed yellow lines. Histamine and GABA in the $\beta3^{+}/\alpha4^{-}$ pocket are taken from the α4β3δ + GABA + histamine structure. THIP in the $\beta3^{+}/\alpha4^{-}$ and $\delta^{+}/\beta3^{-}$ pocket is taken from the α4β3δ + THIP + histamine structure. Histamine in the $\beta3^{+}/\beta3^{-}$ pocket is taken from the α4β3δ + histamine structure. HEPES in the $\beta3^{+}/\beta3^{-}$ pocket is taken from the "apo" α4β3δstructure. GABA in the $\beta3^{+}/\gamma2^{-}$ pocket is taken from the α4β3γ2 + GABA structure. Chain IDs represented in the panels are given as capital letters next to the subunit type.

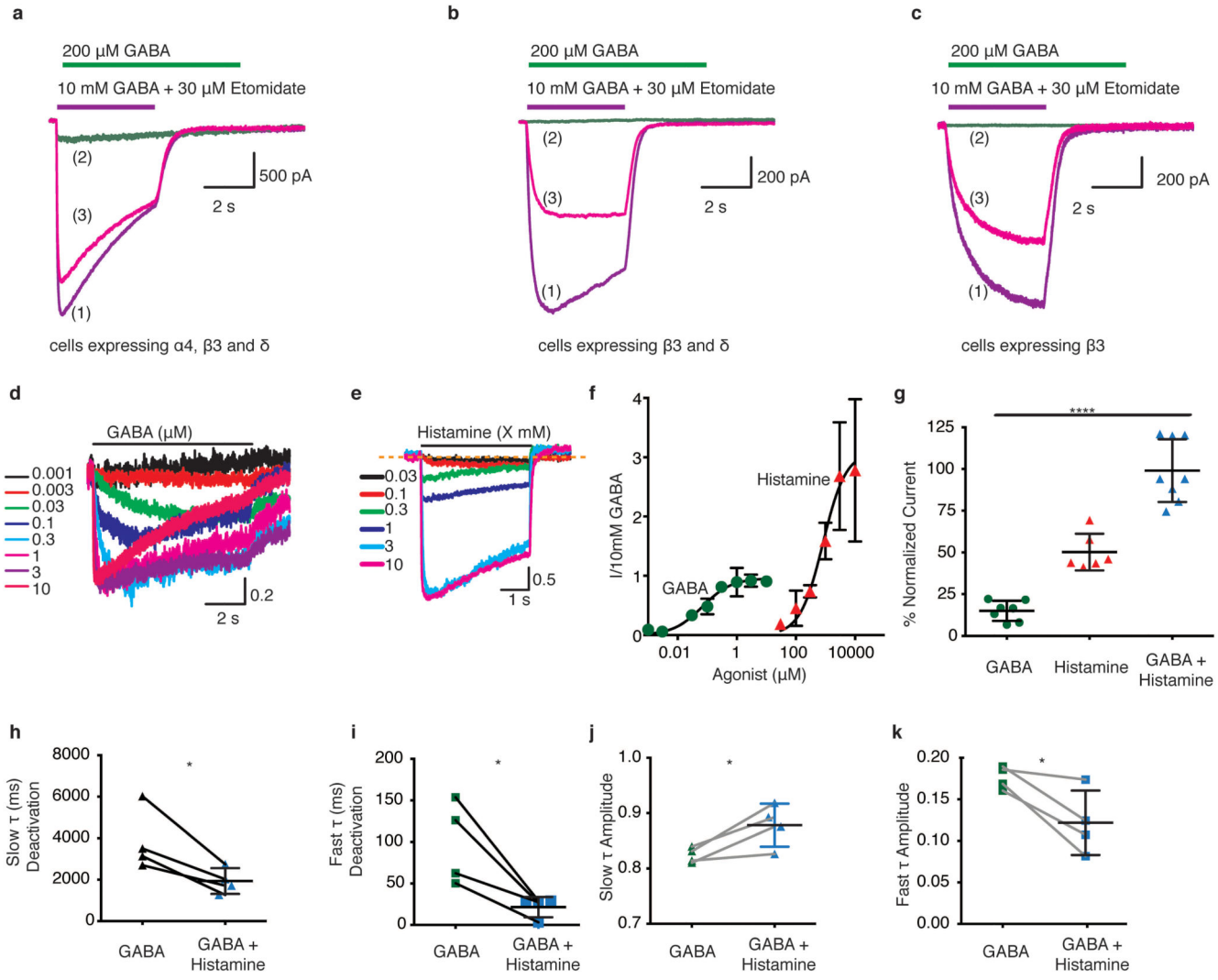

Extended Data Figure 4. Characterizing GABA and histamine effects on $GABA_A$ receptors composed of α4, β3 and δ subunits.

a-c, Unlike α4β3δ receptors (a), β3δ (b) and β3 (c) receptors are not gated by 200 μM GABA. Representative current traces from three successive pulses separated by 1 minute: (1) 4 s pulse of 10 mM GABA plus 30 μM Etomidate (total current, purple); (2) 8 s pulse of 200 μM GABA (green), and (3) repeat of pulse (1) (pink). These pulses are applied to: **a,** cells co-expressing α4, β3 and δ subunits; **b,** cells co-expressing β3 and δ subunits; **c,**

Europe PMC Funders Author Manuscripts

Europe PMC Funders Author Manuscripts

cells expressing the β3 subunit alone. **d-e,** Representative currents normalized to 10 mM GABA currents in the same cell were obtained with varying concentration of (a) GABA (0.001 –10 μM, n = 38 cells with 3-8 cells for each concentration) or (b) histamine (0.03 – 10 mM, n = 31 cells with 3-8 cells for each concentration). In panel **e**, orange dashed line denotes the baseline. **f,** Hill plot of peak amplitude obtained with the normalized currents from (a) and (b) plotted against agonist concentration. The EC50 for GABA was 69.3 nM (95% CI 40.5–118.3 nM) and for histamine was 821.2 μM (95% CI 340.5 – 1981.0 μM) and Hill coefficient of 0.9 (95% CI 0.5 –1.3) and 1.1 (95% CI 0.3 –2.0) respectively. **g,** Scatter plot of peak amplitudes of currents shown in Fig. 2d by GABA (10 mM, n = 7 cells) and histamine (10 mM, n = 6 cells) alone or co-applied (n = 8 cells) in the first pulse as a percent of currents elicited by 10 mM GABA + 30 μM Etomidate. One-way ANOVA $P < 0.0001$. **h-k,** Scatter plots of the time constants ( ) and amplitudes for the slow and fast phases of deactivation that were obtained by fitting a double exponential to the falling phase of currents such as those in Fig. 2e (n = 4 cells for each experiments). In every paired experiment, the direction of change was consistent. In the presence of histamine fast and slow time constants decreased significantly (P = 0.03, two-tailed paired *t* test) and the fraction of receptors with slow deactivation increased (P = 0.04, two-tailed paired *t* test). Significance levels compared to controls were determined by ordinary one–way ANOVA or by the Paired Student's *t* test and are denoted as **** $P < 0.0001$ and * $P < 0.05$. Data are presented as mean ± SD.

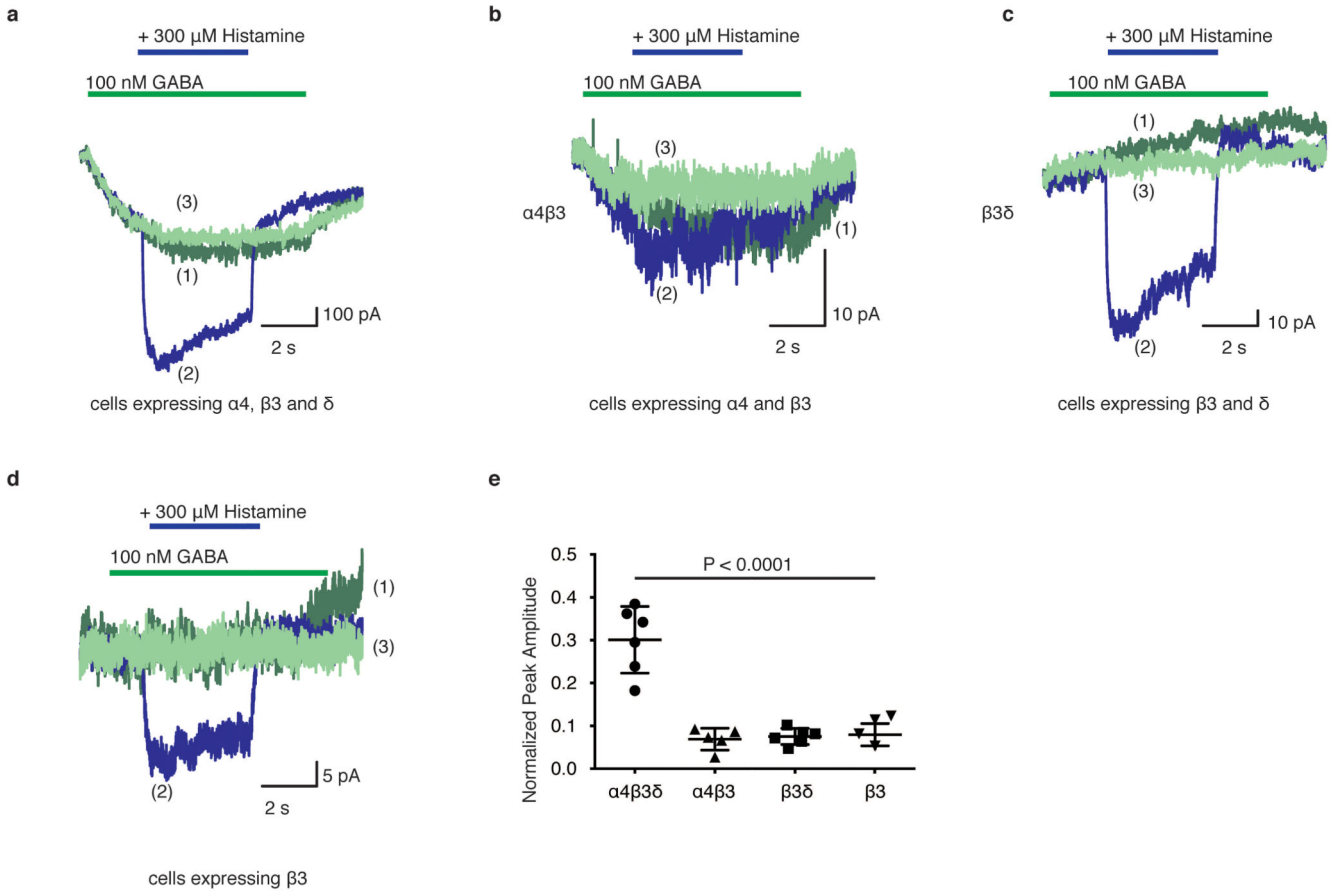

Extended Data Figure 5. GABA and histamine crosstalk happens at the level of individual α4β3δ receptors.

To address the complexity arising from the presence of multiple receptor subtypes, we investigated the modulation of 100 nM GABA currents by 300 µM histamine in cells expressing different combinations of α4, β3 and δ subunits. We first established that 100 nM GABA robustly activates currents in α4β3δ cells (n = 6 cells) (**a**), barely in α4β3 (n = 5 cells) (**b**) and not in β3δ (n = 4 cells) (**c**) or β3 cells (n = 6 cells) (**d**). Histamine at 300 µM robustly enhances the GABA current in 4 3 cells but only modestly in the α4β3, β3δ and β3 cells. The modest enhancement is attributable to histamine currents alone (e.g., from the β3δ or β3-homomeric subtypes). Representative current traces from three successive pulses separated by 1 minute: (1) 8 s pulse of 100 nM GABA (dark green); (2) 8 s pulse of 100 nM GABA with a 4s notch of 300 µM histamine added after two seconds (blue), and (3) 8 s pulse of 100 nM GABA (light green). Finally, to open all receptor isoforms, a normalization pulse of (10 mM GABA + 30 µM etomidate) was applied. **e,** Histamine enhances GABA current strongly only in 4 3 receptors ($P < 0.0001$, one-way ANOVA). Scatter plot shows peak current amplitudes of the blue traces in panels **a-d,** normalized to the total cell current (10 mM GABA + 30 µM etomidate). Data are presented as mean ± SD. Sample size is the same as in panels **a-d**.

Europe PMC Funders Author Manuscripts

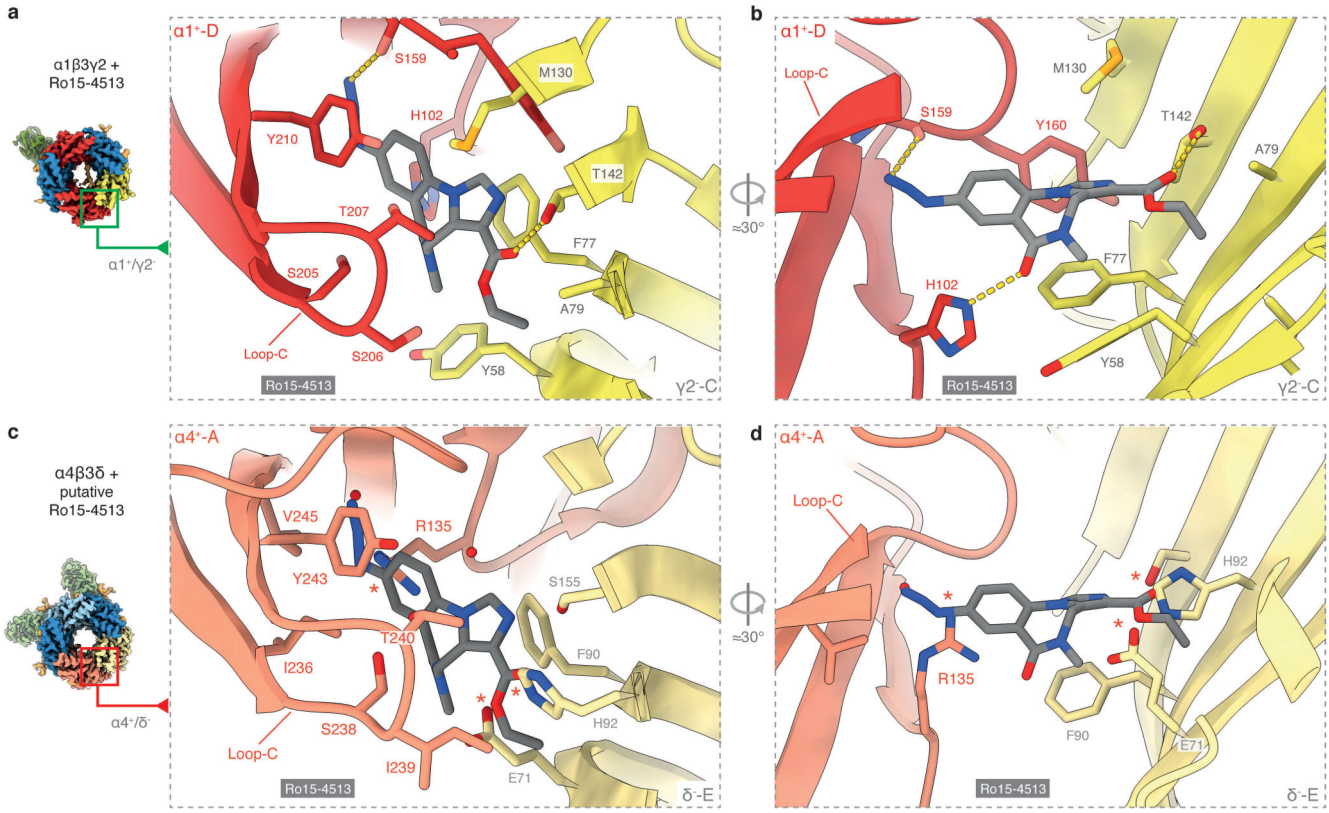

Extended Data Figure 6. Ro15-4513 cannot bind to the $\alpha4^+/\delta^-$ interface.

a-b, Two views of Ro15-4513 bound in the$\alpha1^+/\gamma2^-$ benzodiazepine pocket of an $\alpha1\beta3\gamma2$ receptor. **c-d,** Equivalent views of an $\alpha4\beta3\delta$ receptor show that clashes with the side chains of R135 ($\alpha4^+$), E71 and H92 (δ^-) prevent Ro15-4513 (and, likely, any benzodiazepine ligand) from binding to the $\alpha4^+/\delta^-$ interface in the same mode as observed in $\alpha1\beta3\gamma2$.

Europe PMC Funders Author Manuscripts

Europe PMC Funders Author Manuscripts

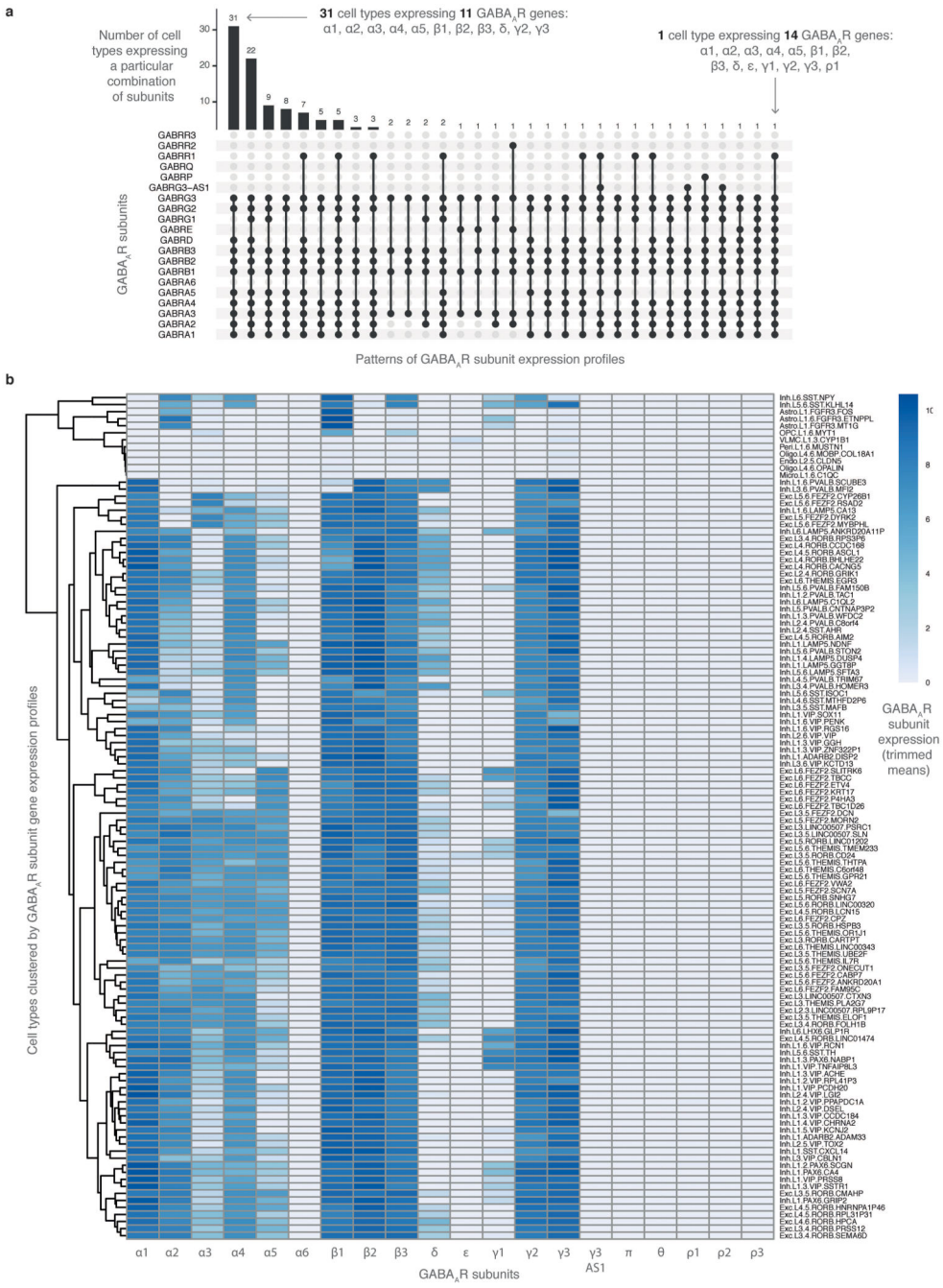

Extended Data Figure 7. Single-cell expression patterns of GABA$_A$R subunits in the human cortex.

a, Grouping cortical cell types by their GABA$_A$R subunit expression. The majority of cell types (31) expresses a combination of 11 different GABA$_A$R subunits, including 1-5, 1-3, and 2-3. Cell type "Exc L5-6 THEMIS THTPA" expresses the highest number of subunits (14): 1-5, 1-3,, 1-3 and 1. Expression in this panel is binarized such that any subunit with a trimmed mean of summed intron and exon counts larger than 0 count per million (CPM) is considered as expressed (Methods). **b,** Heat map showing trimmed means of CPMs for every

GABA$_A$R subunit across individual cell types in the human cortex. Cell types are clustered by their gene expression profiles.

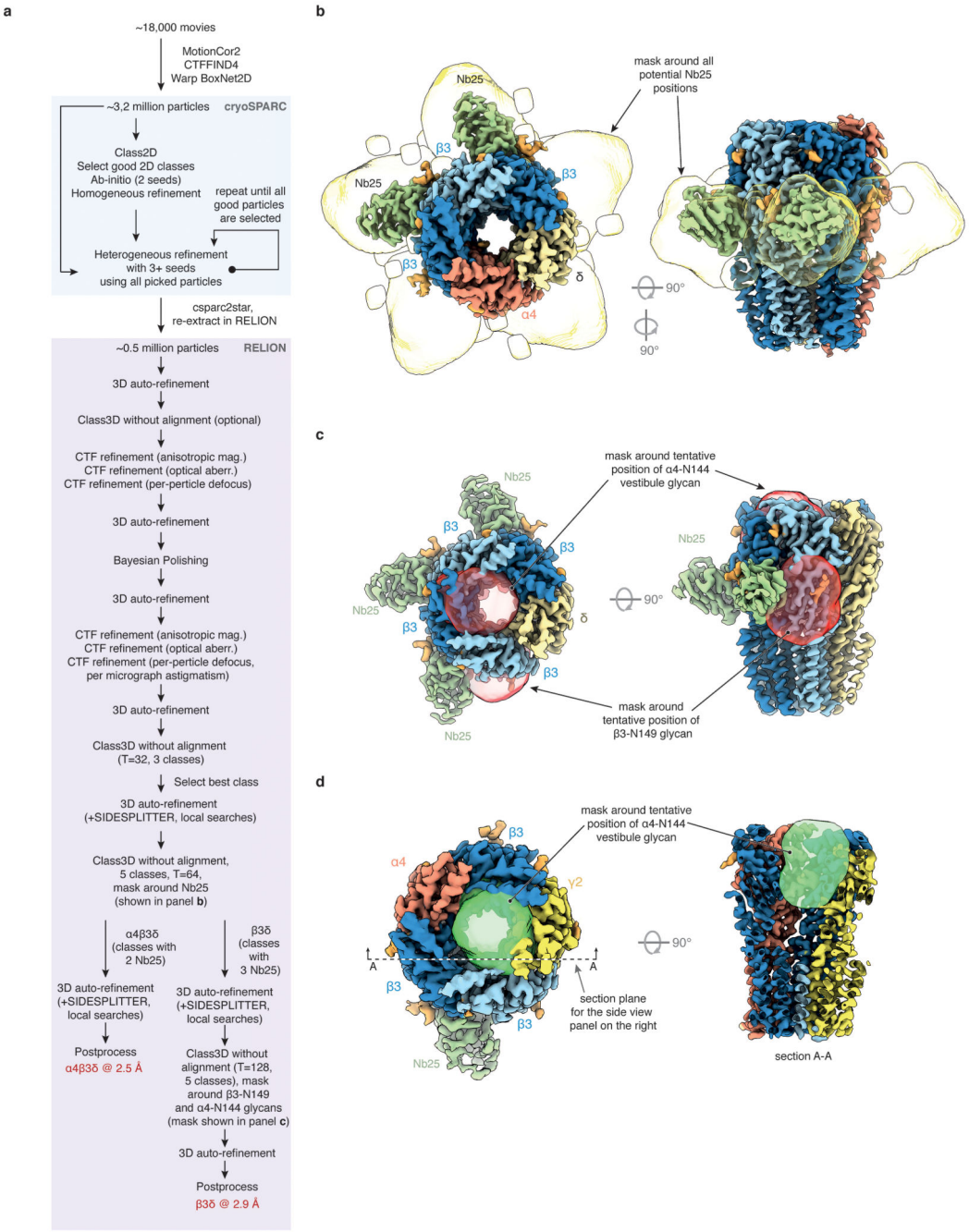

Extended Data Figure 8. Cryo-EM data processing strategy.

a, A typical cryo-EM data processing workflow. The numbers in this case are derived from the α4β3δ "apo" (+HEPES) dataset. **b,** Soft mask used to separate receptors with 2 or 3 Nb25 bound, which largely (but not completely) separates α4β3δ and β3δ receptors. The separation is incomplete in all cases because Nb25 may also bind weakly to the $\beta3^+/\alpha4^-$

interface. **c,** To further separate α4β3δ and β3δ receptors, a soft mask around the putative position of the vestibule glycan on the α4 subunit and the putative position of the N149 glycan on the β3 subunit is used. **d,** Soft mask around the α4 vestibule glycan used to separate α4β3γ2 from β3γ2 receptor subtypes.

Extended Data Table 1
Cryo-EM data collection parameters

	α4β3δ/β3δ apo	**α4β3δ/β3δ + GABA + HSM**	**α4β3γ2/ β3γ2 + GABA**	**α4β3δ/β3δ + THIP + HSM**	**α4β3δ/β3δ + GABA + HSM + Ro15-4513**	**αIβ3γ2 + Ro15-4513**
Data collection and processing						
Microscope	MRC LMB	BiocEM	BiocEM	BiocEM	BiocEM	BiocEM
	Krios G3	Krios G3	Krios G3	Krios G3	Krios G3	Krios G3
Electron Gun	XFEG	XFEG	XFEG	XFEG	XFEG	XFEG
Detector	K3	K3	K3	K3	K3	Falcon 3
Magnification	130K	130K	130K	130K	130K	75K
Energy filter slit width (eV)	20	20	20	20	20	-
Voltage (kV)	300	300	300	300	300	300
Flux on detector (e^- pix/sec)	14.27	15.3	15.4	15.35	15.35	0.55
Electron exposure on sample ($e^-/Å^2$)	40	47.2	47.46	47.31	46.76	28
Target defocus range (μm)	0.9-1.7	0.7-2.1	0.7-2.1	0.7-2.1	0.7-2.1	0.7-2.1
Calibrated pixel size (Å)	0.325 (super-res)	0.326 (super-res)	0.326 (super-res)	0.326 (super-res)	0.326 (super-res)	1.06
Symmetry imposed	Cl	Cl	Cl	Cl	Cl	Cl
Number of collected movies	18254	11562	14346	6437	10546	689
Initial particle images (no.)	3178273	1408073	1579250	718355	1633310	320747
Final particle images	68547 (α4β3δ)	37979 (α4β3δ)	55567 (α4β3γ2)	61854 (α4β3δ)	117439 (α4β3δ)	119901
(no.)	19178 (β3δ)	24240 (β3δ)	65867 (β3γ2)	9667(β3δ)	92694 (α4β3δ closed)	
Map resolution at	2.5 (α4β3δ)	3.0 (α4β3δ) **	3.0 (α4β3γ2)	2.9 (α4β3δ)	2.8 (α4β3δ) *	2.7
FSC=0.143 (Å)	2.9 (β3δ)	3.1 (β3δ)	3.l (β3γ2)	3.4 (β3δ)	2.9 (α4β3δ closed)	
EMPIAR code	10913	10914	10909	10910	10911	10912

* Because Ro15-4513 did not bind, particles from this dataset were combined with particles from GABA + HSM dataset

** to yield the final map of α4β3δ + GABA + HSM to 2.7 Å resolution.

Extended Data Table 2
Refinement and validation statistics

Structure	α4β3δ apo (+HEPES)	β3δ apo (+HEPES)	α4β3δ + GABA + histamine	β3δ + histamine	α4β3δ + histamine	α4β3γ2 + GABA	β3γ2 + GABA	α4β3δ + THIP + histamine	β3δ THI hista
EMDB ID	EMD-14067	EMD-14068	EMD-14069	EMD-14070	EMD-14071	EMD-14072	EMD-14073	EMD-14074	EMD
PDB IB	7QN5	7QN6	7QN7	7QN8	7QN9	7QNA	7QNB	7QNC	7QN
Map resolution refined against (Å)	2.5	2.9	2.7	3.1	2.9	3.0	3.1	2.9	3.4
Map sharpening	0	0	0	0	0	0	0	0	0
B factor (Å ^{2})									
Model composition									
Non-hydrogen atoms	16049	16822	15919	16756	15697	14777	14793	15862	1681
Protein residues	1881	1995	1881	1992	1889	1763	1767	1901	1995
Waters	174	-	3	-	-	-	-	-	-
Ions	3	-	-	-	-	-	-	-	-
Glycans	370	370	412	370	334	356	295	412	370
Ligands	30	45	23	24	24	7	7	36	40
Lipids	80	-	116	-	10	-	-	30	-
Isotropic *B* factors (Å ^{2})									
Protein	77	82	94	100	104	106	116	98	129
Waters	57	-	88	-	-	-	-	-	-
Ions	58	-	-	-	-	-	-	-	-
Glycans	98	104	119	Ill	119	149	147	116	133
Ligands	53	49	71	70	81	97	135	73	34
Lipids	96	-	108	-	114	-	-	118	-
R.m.s. deviations									
Bond lengths (Å)	0.002	0.001	0.002	0.002	0.002	0.002	0.002	0.002	0.00
Bond angles (°)	0.497	0.382	0.479	0.380	0.578	0.395	0.386	0.486	0.37
Validation									
MolProbity score	1.16	1.27	1.15	1.18	1.37	1.24	1.29	1.09	1.25
Clashscore	3.76	5.05	3.53	3.93	6.25	4.65	5.43	2.98	4.79
Poor rotamers (%)	0.36	0.39	0.54	0.34	0.48	0.76	0.56	0.48	0.45
Ramachandran plot									
Favored (%)	98.38	99.08	98.27	99.49	97.90	98.85	98.34	98.27	99.3
Allowed (%)	1.62	0.92	1.73	0.51	2.10	1.15	1.66	1.73	0.61
Disallowed (%)	0.00	0.00	0.00	0.00	0.00	0.00	0.00	0.00	0.00

RMS deviations are from REFMAC [51] . Average B factors are calculated with average_b.py plugin in PyMOL. Other values are calculated by MolProbity [52] from the PHENIX 1.19.2 package [53] .

Supplementary Material

Refer to Web version on PubMed Central for supplementary material.

Acknowledgments

The authors thank M. Madan Babu, D. Barford, T. Blundell, R. Calinescu, A. B. Kleist, A. Murzin, D. Malinverni, C. J. Russo, N. Unwin and the members of Aricescu lab for helpful discussions and comments on this work; V. B. Kasaragod for help with model building; T. Nakane and K. Yamashita for help with data processing; J. Grimmett and T. Darling for support with scientific computing; S. Chen, G. Cannone, G. Sharov, A. Yeates and B. Ahsan for electron microscopy support; T. Uchanski, E. Pardon and J. Steyaert and for the Mb192 megabody. Cryo-EM datasets were collected at the MRC-LMB and Cambridge University Department of Biochemistry EM (BiocEM) facilities. We acknowledge funding from the UK Medical Research Council (MR/L009609/1 and MC_UP_1201/15 to ARA), National Institute for General Medical Sciences (1R01-GM135550 to KWM and ARA), the Department of Anesthesia, Critical Care & Pain Medicine at Massachusetts General Hospital (KWM), MRC LMB and Cambridge Trust (LMB Cambridge Scholarship to AS and KN), School of Clinical Medicine, University of Cambridge (MB/PhD fellowship to AS); Boehringer Ingelheim Fonds (PhD Fellowship to JM). The cryo-EM Facility at the Department of Biochemistry is funded by the Wellcome Trust (206171/Z/17/Z; 202905/Z/16/Z) and the University of Cambridge.

Data availability

Atomic coordinates for the $GABA_AR$ models reported here have been deposited to the Protein Data Bank with accession codes 7QN5-9 and 7QNA-E, and the cryo-EM density maps have been deposited in the Electron Microscopy Data Bank with accession codes EMD-14067 to EMD-14076. Raw movies of all datasets have been deposited in the Electron Microscopy Public Image Archive with accession codes EMPIAR-10909 to EMPIAR-10914. Coordinate files used during model building can be found in the Protein Data Bank under the accession codes 7A5V and 6HUG. scRNAseq data used in the study is available from Allen Brain Map: https://portal.brain-map.org/atlases-and-data/rnaseq/human-multiple-cortical-areas-smart-seq

Code availability

Scripts for scRNA-seq analysis and for running and analysing receptor assembly simulations are available at www.github.com/andrijasente/GABA-differential-assembly.

References

1. Sigel E, Steinmann ME. Structure, function, and modulation of GABA(A) receptors. J Biol Chem. 2012; 287: 40224–40231. DOI: 10.1074/jbc.R112.386664 [PubMed: 23038269]
2. Sieghart W, Sperk G. Subunit composition, distribution and function of GABA(A) receptor subtypes. Curr Top Med Chem. 2002; 2: 795–816. DOI: 10.2174/1568026023393507 [PubMed: 12171572]
3. Sieghart W, Savic MM. International Union of Basic and Clinical Pharmacology. CVI: GABAA Receptor Subtype- and Function-selective Ligands: Key Issues in Translation to Humans. Pharmacol Rev. 2018; 70: 836–878. DOI: 10.1124/pr.117.014449 [PubMed: 30275042]
4. Zhu S, et al. Structure of a human synaptic GABAA receptor. Nature. 2018; 559: 67–72. DOI: 10.1038/s41586-018-0255-3 [PubMed: 29950725]
5. Phulera S, et al. Cryo-EM structure of the benzodiazepine-sensitive alpha1beta1gamma2S tri-heteromeric GABAA receptor in complex with GABA. Elife. 2018; 7 doi: 10.7554/eLife.39383

6. Laverty D, et al. Cryo-EM structure of the human alpha1beta3gamma2 GABAA receptor in a lipid bilayer. Nature. 2019; 565: 516–520. DOI: 10.1038/s41586-018-0833-4 [PubMed: 30602789]
7. Masiulis S, et al. GABAA receptor signalling mechanisms revealed by structural pharmacology. Nature. 2019; 565: 454–459. DOI: 10.1038/s41586-018-0832-5 [PubMed: 30602790]
8. Tasic B, et al. Shared and distinct transcriptomic cell types across neocortical areas. Nature. 2018; 563: 72–78. DOI: 10.1038/s41586-018-0654-5 [PubMed: 30382198]
9. Hodge RD, et al. Conserved cell types with divergent features in human versus mouse cortex. Nature. 2019; 573: 61–68. DOI: 10.1038/s41586-019-1506-7 [PubMed: 31435019]
10. Wisden W, Laurie DJ, Monyer H, Seeburg PH. The distribution of 13 GABAA receptor subunit mRNAs in the rat brain. I. Telencephalon, diencephalon, mesencephalon. J Neurosci. 1992; 12: 1040–1062. [PubMed: 1312131]
11. Nusser Z, Sieghart W, Somogyi P. Segregation of different GABAA receptors to synaptic and extrasynaptic membranes of cerebellar granule cells. J Neurosci. 1998; 18: 1693–1703. [PubMed: 9464994]
12. Pearce RA. Physiological evidence for two distinct GABAA responses in rat hippocampus. Neuron. 1993; 10: 189–200. DOI: 10.1016/0896-6273(93)90310-n [PubMed: 8382497]
13. Baude A, Sequier JM, McKernan RM, Olivier KR, Somogyi P. Differential subcellular distribution of the alpha 6 subunit versus the alpha 1 and beta 2/3 subunits of the GABAA/benzodiazepine receptor complex in granule cells of the cerebellar cortex. Neuroscience. 1992; 51: 739–748. DOI: 10.1016/0306-4522(92)90513-2 [PubMed: 1336825]
14. Farrant M, Nusser Z. Variations on an inhibitory theme: phasic and tonic activation of GABA(A) receptors. Nat Rev Neurosci. 2005; 6: 215–229. DOI: 10.1038/nrn1625 [PubMed: 15738957]
15. Brickley SG, Mody I. Extrasynaptic GABA(A) receptors: their function in the CNS and implications for disease. Neuron. 2012; 73: 23–34. DOI: 10.1016/j.neuron.2011.12.012 [PubMed: 22243744]
16. Scholze P, et al. Two Distinct Populations of alpha1alpha6-Containing GABAA-Receptors in Rat Cerebellum. Front Synaptic Neurosci. 2020; 12 591129 doi: 10.3389/fnsyn.2020.591129 [PubMed: 33123001]
17. Barrera NP, et al. Atomic force microscopy reveals the stoichiometry and subunit arrangement of the alpha4beta3delta GABA(A) receptor. Mol Pharmacol. 2008; 73: 960–967. DOI: 10.1124/mol.107.042481 [PubMed: 18079275]
18. Patel B, Mortensen M, Smart TG. Stoichiometry of delta subunit containing GABA(A) receptors. Br J Pharmacol. 2014; 171: 985–994. DOI: 10.1111/bph.12514 [PubMed: 24206220]
19. Wagoner KR, Czajkowski C. Stoichiometry of expressed alpha(4)beta(2)delta gamma-aminobutyric acid type A receptors depends on the ratio of subunit cDNA transfected. J Biol Chem. 2010; 285: 14187–14194. DOI: 10.1074/jbc.M110.104257 [PubMed: 20233712]
20. Botzolakis EJ, et al. Comparison of gamma-Aminobutyric Acid, Type A (GABAA), Receptor alphabetagamma and alphabetadelta Expression Using Flow Cytometry and Electrophysiology: EVIDENCE FOR ALTERNATIVE SUBUNIT STOICHIOMETRIES AND ARRANGEMENTS. J Biol Chem. 2016; 291: 20440–20461. DOI: 10.1074/jbc.M115.698860 [PubMed: 27493204]
21. Zhou X, et al. High-level production and purification in a functional state of an extrasynaptic gamma-aminobutyric acid type A receptor containing alpha4beta3delta subunits. PLoS One. 2018; 13 e0191583 doi: 10.1371/journal.pone.0191583 [PubMed: 29352320]
22. Eaton MM, et al. gamma-aminobutyric acid type A alpha4, beta2, and delta subunits assemble to produce more than one functionally distinct receptor type. Mol Pharmacol. 2014; 86: 647–656. DOI: 10.1124/mol.114.094813 [PubMed: 25238745]
23. Nakane T, et al. Single-particle cryo-EM at atomic resolution. Nature. 2020; 587: 152–156. DOI: 10.1038/s41586-020-2829-0 [PubMed: 33087931]
24. Saras A, et al. Histamine action on vertebrate GABAA receptors: direct channel gating and potentiation of GABA responses. J Biol Chem. 2008; 283: 10470–10475. DOI: 10.1074/jbc.M709993200 [PubMed: 18281286]
25. Wongsamitkul N, et al. alpha subunits in GABAA receptors are dispensable for GABA and diazepam action. Sci Rep. 2017; 7 15498 doi: 10.1038/s41598-017-15628-7 [PubMed: 29138471]

26. Taylor PM, et al. Identification of amino acid residues within GABA(A) receptor beta subunits that mediate both homomeric and heteromeric receptor expression. J Neurosci. 1999; 19: 6360–6371. [PubMed: 10414965]
27. Bianchi MT, Clark AG, Fisher JL. The wake-promoting transmitter histamine preferentially enhances alpha-4 subunit-containing GABAA receptors. Neuropharmacology. 2011; 61: 747–752. DOI: 10.1016/j.neuropharm.2011.05.020 [PubMed: 21640733]
28. Lee HJ, et al. A pharmacological characterization of GABA, THIP and DS2 at binary alpha4beta3 and beta3delta receptors: GABA activates beta3delta receptors via the beta3(+)delta(-) interface. Brain Res. 2016; 1644: 222–230. DOI: 10.1016/j.brainres.2016.05.019 [PubMed: 27181518]
29. Miller PS, Aricescu AR. Crystal structure of a human GABAA receptor. Nature. 2014; 512: 270–275. DOI: 10.1038/nature13293 [PubMed: 24909990]
30. Hoerbelt P, et al. Mutagenesis and computational docking studies support the existence of a histamine binding site at the extracellular beta3+beta3-interface of homooligomeric beta3 GABAA receptors. Neuropharmacology. 2016; 108: 252–263. DOI: 10.1016/j.neuropharm.2016.04.042 [PubMed: 27140694]
31. Falch E, Krogsgaard-Larsen P. The binding of the GABA agonist [3H]THIP to rat brain synaptic membranes. J Neurochem. 1982; 38: 1123–1129. DOI: 10.1111/j.1471-4159.1982.tb05357.x [PubMed: 6278083]
32. Wafford KA, Ebert B. Gaboxadol--a new awakening in sleep. Curr Opin Pharmacol. 2006; 6: 30–36. DOI: 10.1016/j.coph.2005.10.004 [PubMed: 16368265]
33. Hanchar HJ, et al. Ethanol potently and competitively inhibits binding of the alcohol antagonist Ro15-4513 to alpha4/6beta3delta GABAA receptors. Proc Natl Acad Sci U S A. 2006; 103: 8546–8551. DOI: 10.1073/pnas.0509903103 [PubMed: 16581914]
34. Wallner M, Hanchar HJ, Olsen RW. Low-dose alcohol actions on alpha4beta3delta GABAA receptors are reversed by the behavioral alcohol antagonist Ro15-4513. Proc Natl Acad Sci U S A. 2006; 103: 8540–8545. DOI: 10.1073/pnas.0600194103 [PubMed: 16698930]
35. Olsen RW, Hanchar HJ, Meera P, Wallner M. GABAA receptor subtypes: the “one glass of wine” receptors. Alcohol. 2007; 41: 201–209. DOI: 10.1016/j.alcohol.2007.04.006 [PubMed: 17591543]
36. Linden AM, et al. Ro 15-4513 Antagonizes Alcohol-Induced Sedation in Mice Through alphabetagamma2-type GABA(A) Receptors. Front Neurosci. 2011; 5: 3. doi: 10.3389/fnins.2011.00003 [PubMed: 21270945]
37. Storustovu SI, Ebert B. Pharmacological characterization of agonists at delta-containing GABAA receptors: Functional selectivity for extrasynaptic receptors is dependent on the absence of gamma2. J Pharmacol Exp Ther. 2006; 316: 1351–1359. DOI: 10.1124/jpet.105.092403 [PubMed: 16272218]
38. Brown N, Kerby J, Bonnert TP, Whiting PJ, Wafford KA. Pharmacological characterization of a novel cell line expressing human alpha(4)beta(3)delta GABA(A) receptors. Br J Pharmacol. 2002; 136: 965–974. DOI: 10.1038/sj.bjp.0704795 [PubMed: 12145096]
39. Marti-Solano M, et al. Combinatorial expression of GPCR isoforms affects signalling and drug responses. Nature. 2020; 587: 650–656. DOI: 10.1038/s41586-020-2888-2 [PubMed: 33149304]
40. Rudolph U, Knoflach F. Beyond classical benzodiazepines: novel therapeutic potential of GABAA receptor subtypes. Nat Rev Drug Discov. 2011; 10: 685–697. DOI: 10.1038/nrd3502 [PubMed: 21799515]
41. Bencsits E, Ebert V, Tretter V, Sieghart W. A significant part of native gamma-aminobutyric AcidA receptors containing alpha4 subunits do not contain gamma or delta subunits. J Biol Chem. 1999; 274: 19613–19616. DOI: 10.1074/jbc.274.28.19613 [PubMed: 10391897]
42. Levitan ES, et al. Structural and functional basis for GABAA receptor heterogeneity. Nature. 1988; 335: 76–79. DOI: 10.1038/335076a0 [PubMed: 2842688]
43. Brickley SG, Cull-Candy SG, Farrant M. Single-channel properties of synaptic and extrasynaptic GABAA receptors suggest differential targeting of receptor subtypes. J Neurosci. 1999; 19: 2960–2973. [PubMed: 10191314]
44. Mertens S, Benke D, Mohler H. GABAA receptor populations with novel subunit combinations and drug binding profiles identified in brain by alpha 5- and delta-subunit-specific immunopurification. J Biol Chem. 1993; 268: 5965–5973. [PubMed: 8383681]

45. Fritschy JM, et al. Five subtypes of type A gamma-aminobutyric acid receptors identified in neurons by double and triple immunofluorescence staining with subunit-specific antibodies. Proc Natl Acad Sci U S A. 1992; 89: 6726–6730. DOI: 10.1073/pnas.89.15.6726 [PubMed: 1323116]
46. Duggan MJ, Pollard S, Stephenson FA. Immunoaffinity purification of GABAA receptor alpha-subunit iso-oligomers. Demonstration of receptor populations containing alpha 1 alpha 2, alpha 1 alpha 3, and alpha 2 alpha 3 subunit pairs. J Biol Chem. 1991; 266: 24778–24784. [PubMed: 1662216]
47. Owens DF, Kriegstein AR. Is there more to GABA than synaptic inhibition? Nat Rev Neurosci. 2002; 3: 715–727. DOI: 10.1038/nrn919 [PubMed: 12209120]
48. Datta D, Arion D, Lewis DA. Developmental Expression Patterns of GABAA Receptor Subunits in Layer 3 and 5 Pyramidal Cells of Monkey Prefrontal Cortex. Cereb Cortex. 2015; 25: 2295–2305. DOI: 10.1093/cercor/bhu040 [PubMed: 24610118]
49. Fatemi SH, Folsom TD, Rooney RJ, Thuras PD. Expression of GABAA alpha2-, beta1- and epsilon-receptors are altered significantly in the lateral cerebellum of subjects with schizophrenia, major depression and bipolar disorder. Transl Psychiatry. 2013; 3 e303 doi: 10.1038/tp.2013.64 [PubMed: 24022508]
50. Mueller TM, Remedies CE, Haroutunian V, Meador-Woodruff JH. Abnormal subcellular localization of GABAA receptor subunits in schizophrenia brain. Transl Psychiatry. 2015; 5 e612 doi: 10.1038/tp.2015.102 [PubMed: 26241350]
51. Murshudov GN, et al. REFMAC5 for the refinement of macromolecular crystal structures. Acta Crystallogr D Biol Crystallogr. 2011; 67: 355–367. DOI: 10.1107/S0907444911001314 [PubMed: 21460454]
52. Chen VB, et al. MolProbity: all-atom structure validation for macromolecular crystallography. Acta Crystallogr D Biol Crystallogr. 2010; 66: 12–21. DOI: 10.1107/S0907444909042073 [PubMed: 20057044]
53. Afonine PV, et al. Real-space refinement in PHENIX for cryo-EM and crystallography. Acta Crystallogr D Struct Biol. 2018; 74: 531–544. DOI: 10.1107/S2059798318006551 [PubMed: 29872004]
54. Reeves PJ, Kim JM, Khorana HG. Structure and function in rhodopsin: a tetracycline-inducible system in stable mammalian cell lines for high-level expression of opsin mutants. Proc Natl Acad Sci U S A. 2002; 99: 13413–13418. DOI: 10.1073/pnas.212519199 [PubMed: 12370422]
55. Elegheert J, et al. Lentiviral transduction of mammalian cells for fast, scalable and high-level production of soluble and membrane proteins. Nat Protoc. 2018; 13: 2991–3017. DOI: 10.1038/s41596-018-0075-9 [PubMed: 30455477]
56. Dostalova Z, et al. Human alpha1beta3gamma2L gamma-aminobutyric acid type A receptors: High-level production and purification in a functional state. Protein Sci. 2014; 23: 157–166. DOI: 10.1002/pro.2401 [PubMed: 24288268]
57. Miller PS, et al. Structural basis for GABAA receptor potentiation by neurosteroids. Nat Struct Mol Biol. 2017; 24: 986–992. DOI: 10.1038/nsmb.3484 [PubMed: 28991263]
58. Uchanski T, et al. Megabodies expand the nanobody toolkit for protein structure determination by single-particle cryo-EM. Nat Methods. 2021; 18: 60–68. DOI: 10.1038/s41592-020-01001-6 [PubMed: 33408403]
59. Russo CJ, Passmore LA. Electron microscopy: Ultrastable gold substrates for electron cryomicroscopy. Science. 2014; 346: 1377–1380. DOI: 10.1126/science.1259530 [PubMed: 25504723]
60. Zheng SQ, et al. MotionCor2: anisotropic correction of beam-induced motion for improved cryo-electron microscopy. Nat Methods. 2017; 14: 331–332. DOI: 10.1038/nmeth.4193 [PubMed: 28250466]
61. Rohou A, Grigorieff N. CTFFIND4: Fast and accurate defocus estimation from electron micrographs. J Struct Biol. 2015; 192: 216–221. DOI: 10.1016/j.jsb.2015.08.008 [PubMed: 26278980]
62. Tegunov D, Cramer P. Real-time cryo-electron microscopy data preprocessing with Warp. Nat Methods. 2019; 16: 1146–1152. DOI: 10.1038/s41592-019-0580-y [PubMed: 31591575]

63. Punjani A, Rubinstein JL, Fleet DJ, Brubaker MA. cryoSPARC: algorithms for rapid unsupervised cryo-EM structure determination. Nat Methods. 2017; 14: 290–296. DOI: 10.1038/nmeth.4169 [PubMed: 28165473]
64. Asarnow D, Palovcak E, Cheng Y. asarnow/pyem: UCSF pyem v0. 2019; 5
65. Scheres SH. RELION: implementation of a Bayesian approach to cryo-EM structure determination. J Struct Biol. 2012; 180: 519–530. DOI: 10.1016/j.jsb.2012.09.006 [PubMed: 23000701]
66. Zivanov J, et al. New tools for automated high-resolution cryo-EM structure determination in RELION-3. Elife. 2018; 7 doi: 10.7554/eLife.42166
67. Zivanov J, Nakane T, Scheres SHW. Estimation of high-order aberrations and anisotropic magnification from cryo-EM data sets in RELION-3.1. IUCrJ. 2020; 7: 253–267. DOI: 10.1107/S2052252520000081
68. Zivanov J, Nakane T, Scheres SHW. A Bayesian approach to beam-induced motion correction in cryo-EM single-particle analysis. IUCrJ. 2019; 6: 5–17. DOI: 10.1107/S205225251801463X
69. Pettersen EF, et al. UCSF Chimera--a visualization system for exploratory research and analysis. J Comput Chem. 2004; 25: 1605–1612. DOI: 10.1002/jcc.20084 [PubMed: 15264254]
70. Ramlaul K, Palmer CM, Nakane T, Aylett CHS. Mitigating local over-fitting during single particle reconstruction with SIDESPLITTER. J Struct Biol. 2020; 211 107545 doi: 10.1016/j.jsb.2020.107545 [PubMed: 32534144]
71. Kucukelbir A, Sigworth FJ, Tagare HD. Quantifying the local resolution of cryo-EM density maps. Nat Methods. 2014; 11: 63–65. DOI: 10.1038/nmeth.2727 [PubMed: 24213166]
72. Naydenova K, Russo CJ. Measuring the effects of particle orientation to improve the efficiency of electron cryomicroscopy. Nat Commun. 2017; 8: 629. doi: 10.1038/s41467-017-00782-3 [PubMed: 28931821]
73. Goddard TD, et al. UCSF ChimeraX: Meeting modern challenges in visualization and analysis. Protein Sci. 2018; 27: 14–25. DOI: 10.1002/pro.3235 [PubMed: 28710774]
74. Waterhouse A, et al. SWISS-MODEL: homology modelling of protein structures and complexes. Nucleic Acids Res. 2018; 46: W296–W303. DOI: 10.1093/nar/gky427 [PubMed: 29788355]
75. Weininger D. SMILES, a chemical language and information system. 1. Introduction to methodology and encoding rules. Journal of chemical information and computer sciences. 1988; 28: 31–36.
76. Emsley P, Cowtan K. Coot: model-building tools for molecular graphics. Acta Crystallogr D Biol Crystallogr. 2004; 60: 2126–2132. DOI: 10.1107/S0907444904019158 [PubMed: 15572765]
77. Nicholls RA, Fischer M, McNicholas S, Murshudov GN. Conformationindependent structural comparison of macromolecules with ProSMART. Acta Crystallogr D Biol Crystallogr. 2014; 70: 2487–2499. DOI: 10.1107/S1399004714016241 [PubMed: 25195761]
78. Forman SA. A hydrophobic photolabel inhibits nicotinic acetylcholine receptors via open-channel block following a slow step. Biochemistry. 1999; 38: 14559–14564. DOI: 10.1021/bi9914457 [PubMed: 10545178]
79. Sente A, Naydenova K. Scripts for Differential assembly diversifies GABAA receptor structures and signaling (v1.0.1). Zenodo. 2022; doi: 10.5281/zenodo.5884871

Europe PMC Funders Author Manuscripts

Europe PMC Funders Author Manuscripts

One sentence summary

An integrative structural biology approach demonstrates how the diverse subunit stoichiometry and arrangement enrich the structure, physiology and pharmacology of $GABA_A$ receptors.

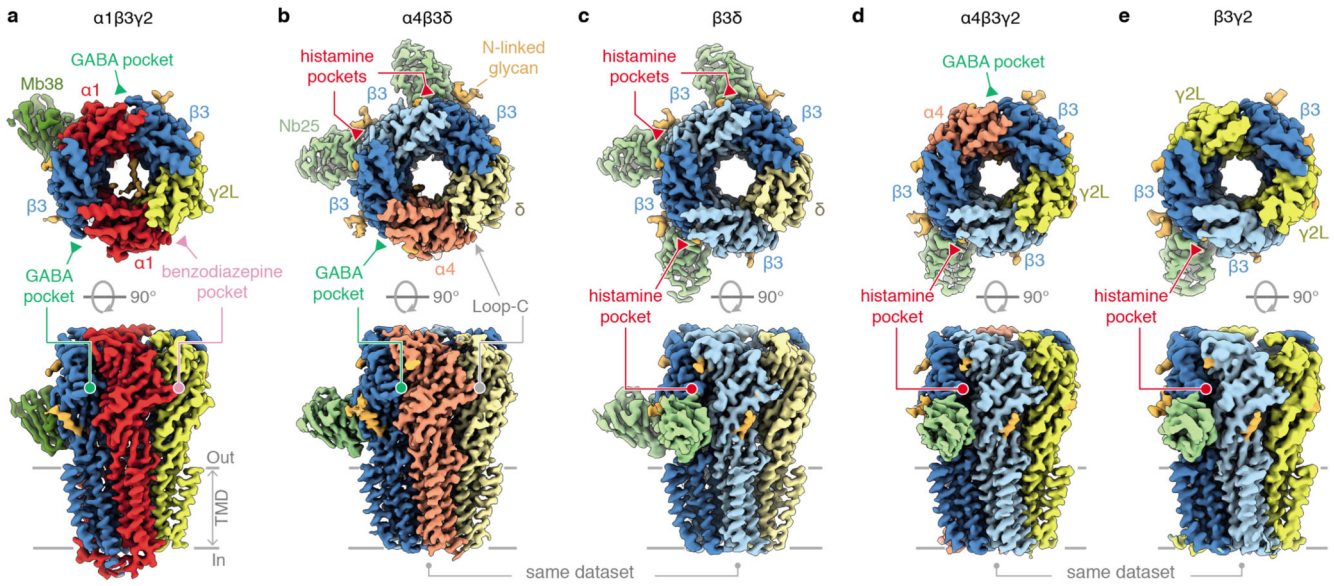

Figure 1. Landscape of differential $GABA_A$ receptor assemblies.

a-e, Structures, subunit arrangements and ligand binding pockets of α1β3γ2 (**a**), α4β3δ (**b**), β3δ solved from the same dataset (**c**), α4β3γ2 (**d**) and β3γ2 $GABA_AR$ solved from the same dataset (**e**).

Europe PMC Funders Author Manuscripts

Europe PMC Funders Author Manuscripts

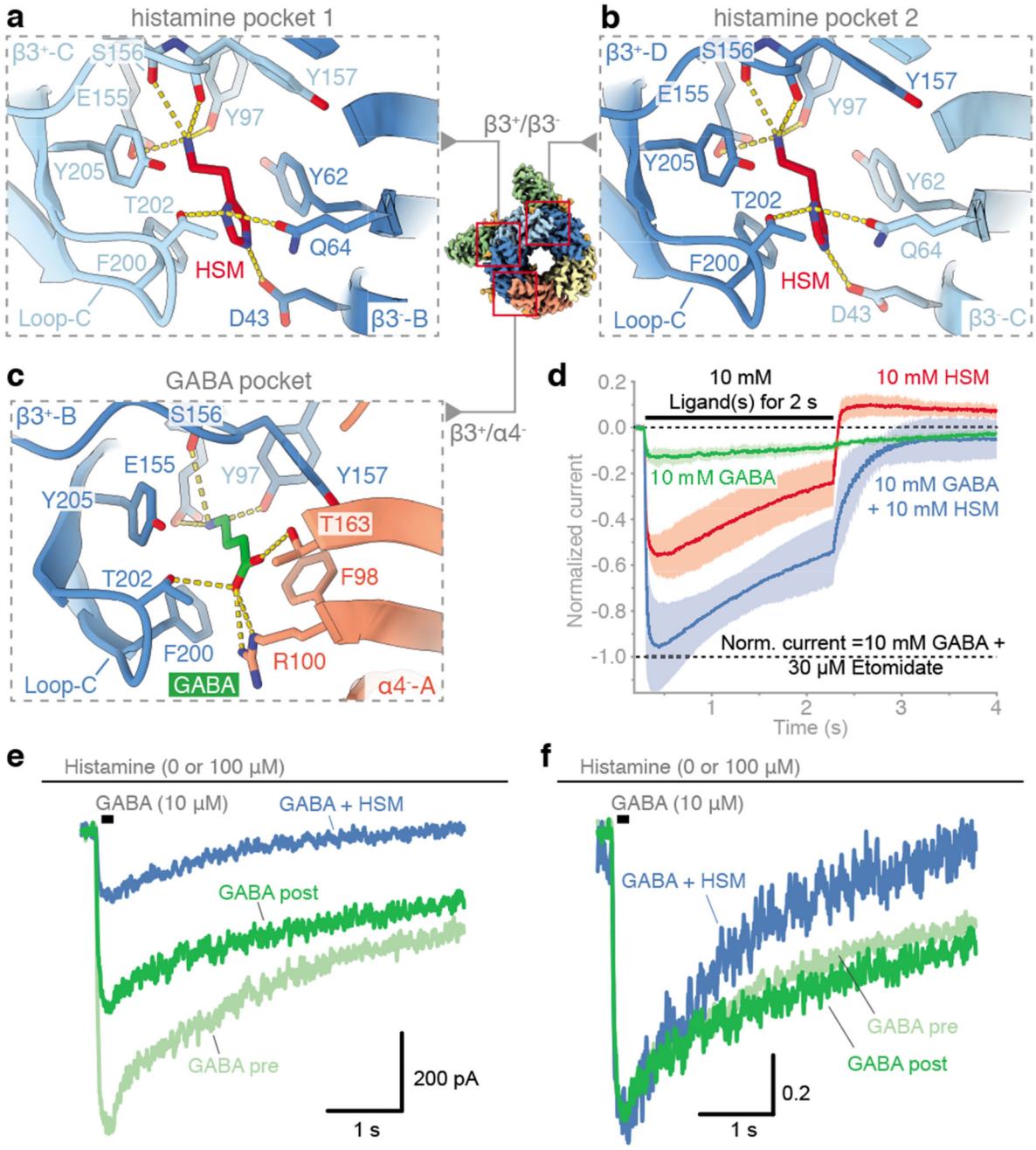

Figure 2. Interplay of GABA and histamine at α4β3δ GABA$_A$R.

a-b, Histamine bound in the two β3$^+$/β3$^-$ agonist pockets. **c,** GABA bound in the β3$^+$/α4$^-$ agonist pocket. **d,** In 4 3 cells, an equimolar mix of GABA and histamine (10mM each) gates more receptors than each ligand applied alone. Superimposed, normalized whole-cell current averaged traces obtained with a two-pulse protocol described in Methods. GABA gated 15.0 ± 6.0 % (n = 7 cells), histamine 50.2 ± 11.0 % (n = 6 cells) and histamine + GABA together 99.0 ± 18.9% (n = 8 cells) of total receptors gated by 10 mM GABA + 30μM Etomidate. Standard deviations were propagated. Statistical analysis is shown in

Europe PMC Funders Author Manuscripts

Extended Data Fig. 4g. **e-f,** Representative deactivating current traces obtained from the same cell by application of a 200 ms pulse of GABA alone, or in the presence of 100 μM histamine (the same current traces normalised as described in Methods are shown in **f**). Pre-application of a low concentration of histamine, where its agonistic action was weak, caused a decrease in peak current amplitude of the deactivating currents by 74.5 ± 11.9 % (n = 4 cells) (**e**) and the deactivation rate became faster, with current reaching 50% of its original value in 1.0 ± 0.4 s (n = 4) instead of 2.7 ± 0.7 s (n = 4 cells; $P = 0.002$, two-tailed paired *t* test) in the absence of histamine (**f**). Statistical analysis of deactivation time constants ( ) and amplitudes is shown in Extended Data Fig. 4h–k. Data are presented as mean ± SD.

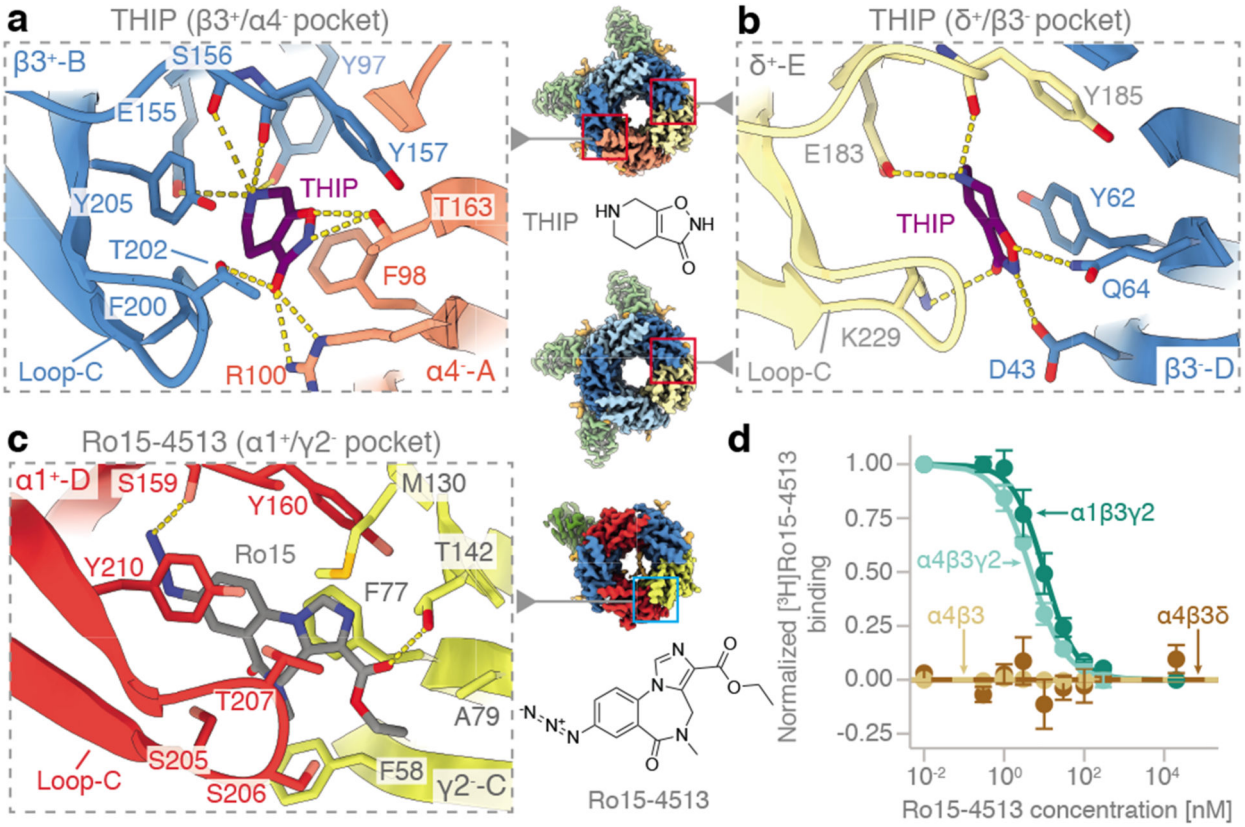

Figure 3. Differential assembly of GABA$_A$R affects drug responses.

a, Inset showing THIP bound in the β3$^+$/α4$^-$ "agonist pocket" of an α4β3δ GABA$_A$R. **b,** THIP coordination in the second binding site, the δ$^+$/β$^-$ "agonist pocket" of an α4β3δ GABA$_A$R. The same binding mode is observed in the second receptor subtype solved from the same dataset, the β3δ receptor. **c,** Ro15-4513 binding mode in the α1$^+$/γ2$^-$ pocket of the α1β3γ2 receptor. **d,** Radioligand assay measuring competition of Ro15-4513 with pre-bound [^{3}H]Ro15-4513 shows that the ligand binds to cells expressing α1, β3, γ2 and α4, β3, γ2 subunits, but not the ones expressing α4, β3, δ or α4, β3 subunits (n = 3 technical repeats for each measurement). Data is presented as mean ± SD.

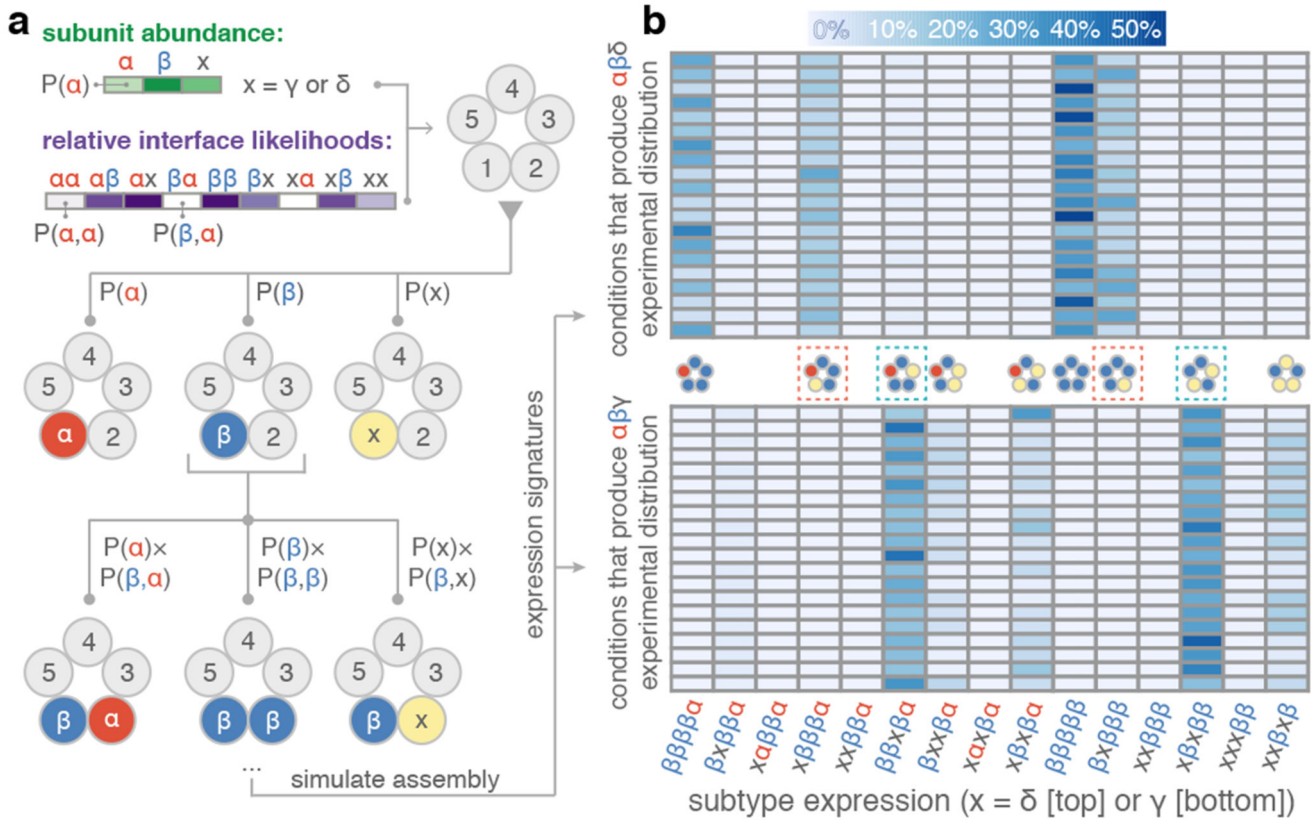

Figure 4. Computational simulations of receptor assembly.

a, Schematic diagram of the simulation process. **b,** Expression of selected $GABA_AR$ subtypes across different simulated conditions. Out of all conditions that favour the expression patterns observed in experimental data from α4β3δ (top) or α4β3γ2 cell line (bottom) (Methods), twenty examples were randomly chosen for display. Here x denotes δ (top) or γ (bottom). Each row represents one simulated condition. The colour scale indicates subtype abundance in each condition. Receptor subtypes expressed across different simulated conditions are shown between the two panels. Experimentally observed subtypes are denoted with dashed boxes (red and blue for α4β3δ and α4β3γ2, respectively).

Europe PMC Funders Author Manuscripts